Blue-emitting SiO_2-coated Si-doped ZnSeS quantum dots conjugated aptamer-molecular beacon as an electrochemical and metal-enhanced fluorescence biosensor for SARS-CoV-2 spike protein

Adegoke, Oluwasesan; Oyinlola, Kayode; Achadu, Ojodomo J.; Yang, Zhugen

Published in:
Analytica Chimica Acta

DOI:
10.1016/j.aca.2023.341926

Publication date:
2023

Analytica Chimica Acta 1281 (2023) 341926

Contents lists available at ScienceDirect

Analytica Chimica Acta

journal homepage: www.elsevier.com/locate/aca

Blue-emitting SiO_2-coated Si-doped ZnSeS quantum dots conjugated aptamer-molecular beacon as an electrochemical and metal-enhanced fluorescence biosensor for SARS-CoV-2 spike protein

Oluwasesan Adegoke [a,*], Kayode Oyinlola [a], Ojodomo J. Achadu [b], Zhugen Yang [c]

[a] Leverhulme Research Centre for Forensic Science, School of Science and Engineering, University of Dundee, Dundee, DD1 4HN, UK
[b] School of Health and Life Sciences, National Horizon Centre, Teesside University, TS1 3BA, Middlesbrough, UK
[c] School of Water, Energy and Environment, Cranfield University, Cranfield, MK43 0AL, UK

HIGHLIGHTS

- Blue-emitting fluorescent SiO_2-coated Si-doped ZnSeS (QDs) were synthesized.
- The QDs was conjugated to an aptamer molecular beacon (Apta-MB).
- Cationic gold nanoparticles (AuNPs) amplified the fluorescence intensity.
- An electrochemical biosensor for SARS-CoV-2 spike (S) protein was developed.
- The QDs-Apta-MB-AuNP detected SARS-CoV-2 S protein in saliva.

GRAPHICAL ABSTRACT

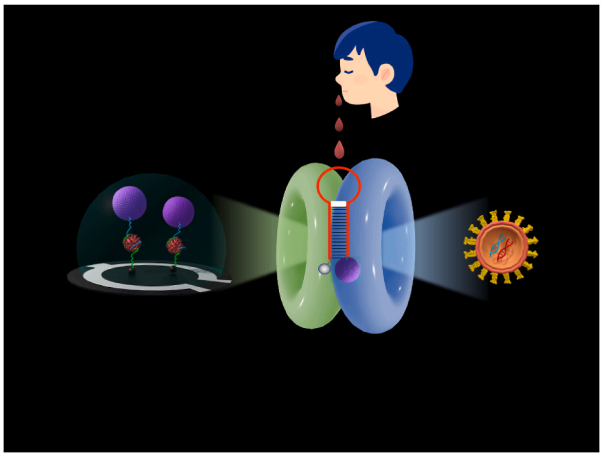

ARTICLE INFO

Handling Editor: Professor Chuck Henry

ABSTRACT

The outbreak of severe acute respiratory syndrome coronavirus 2 (SARS-CoV-2) which was first reported in early January 2020, continues to devastate the worlds public health system. Herein, we report on the development of a novel metal-enhanced fluorescence (MEF) and electrochemical biosensor for SARS-CoV-2 spike (S) protein. To develop the MEF biosensor, SiO_2-coated Si-doped ZnSeS quantum dots (QDs) were newly synthesized and conjugated to an aptamer-molecular beacon (Apta-MB) probe. Thereafter, cationic AuNPs, used as a localised surface plasmon resonance (LSPR) signal amplifier, were self-assembled on the QDs-Apta-MB conjugate to form a QDs-Apta-MB-AuNP probe. To develop the electrochemical biosensor, the QDs-Apta-MB assay was carried out on a carbon nanofiber-modified screen-printed carbon electrode. Cyclic voltammetry (CV), differential pulse voltammetry (DPV) and electrochemical impedance spectroscopy (EIS) were used to characterize the electrode surface whilst spectrophotometric, spectroscopic, fluorescence polarization and electron microscopic techniques

* Corresponding author. Leverhulme Research Centre for Forensic Science, School of Science & Engineering, University of Dundee, Dundee, DD1 4GH, UK.
E-mail address: o.adegoke@dundee.ac.uk (O. Adegoke).

https://doi.org/10.1016/j.aca.2023.341926
Received 1 September 2023; Received in revised form 14 October 2023; Accepted 16 October 2023
Available online 17 October 2023

were used to characterize the materials. Under optimal experimental conditions, the QDs binding to the Apta-MB, quenched the QDs' fluorescence and with SARS-CoV-2 S protein binding to the Apta-MB, LSPR signal from cationic AuNPs of different sizes and shapes were used to tune the fluorescence signal to obtain enhanced sensitivity. On the other hand, using $[Fe(CN)_6]/K^{3-}/^{4-}$ buffered with NaAc-KAc-TrizmaAc-KSCN-Borax as the electrolyte solution, anodic peaks of the QDs from the CV and DPV plots were unravelled. Electrochemical detection of SARS-CoV-2 S protein was accomplished by a systematic increase in the QDs anodic peak current generated from the DPV plots. The limits of detection obtained for the SARS-CoV-2 S protein were 8.9 fg/mL for the QDs-Apta-MB-AuNP MEF probe and ~0.5 pg/mL for the QDs-Apta-MB electrochemical probe. Detection of SARS-CoV-2 S protein in saliva was demonstrated using the QDs-Apta-MB-AuNP MEF probe.

1. Introduction

Semiconductor quantum dots (QDs), graphene QDs and carbon dots are the three most used nanofluorophores in mainstream fluorescence sensing research [1]. Amongst these three, semiconductor QDs has found wider application due to their unique electro-optical properties that arises from their quantum confinement properties [2]. Compared to graphene QDs, carbon dots and organic fluorophore dyes, semiconductor QDs exhibits tuneable, narrow symmetric emission and broad absorption spectra, higher fluorescence quantum yield (QY), excellent photostability, more efficient surface area-to-volume ratio and highly efficient multi-photon light absorbing properties [3]. The large surface area-to-volume ratio properties of QDs, lends the opportunity to dope their surface with metal ions to produce improved photoluminescent properties [4]. Although, QDs have found wide applications across the scientific field of study, most of the QDs used in mainstream sensing research have involved the use of the toxic cadmium (Cd) chalcogenide metal [3]. Due to safety concern, there is a need to develop novel non-Cd based QDs and alleviate the toxicity concern posed by Cd-based QDs.

In terms of sensing techniques, over the past 30 years, fluorescence and electrochemical detection have become one of the dominant sensing technologies in mainstream sensor research [5,6]. Metal-enhanced fluorescence (MEF) is a modified version of fluorescence sensing that represents an alternative way to detect ultralow concentration of target analytes based on the interaction of plasmonic metal nanoparticles (NPs) with nanofluorophores [7,8]. The presence of metallic NPs close to the fluorophore surface, can drastically alter the spectral properties of the fluorophore [7] via localised surface plasmon resonance (LSPR) mediated intensity signal which in turn leads to decrease or increase of the fluorophore's radiative decay rates [8]. The decrease or increase of the fluorophore emission results from interaction of free (or surface plasmon) electrons in the metal with the excited state fluorophore. MEF sensors involving the use of plasmonic silver (Ag) NPs or AuNPs with nanofluorophores have found widespread application in the detection of viruses [9], illicit drugs [10], insecticides [11], bacteria [12], cancer cells [13], and amino acids [14], etc. Thus, in mainstream MEF sensing research, QDs have found wider application as fluorophore reporters and in the development of fluorescence [4,11,12] and electrochemical sensors [15] applicable to the food, biomedical, defence and security and environmental industry.

The outbreak of severe acute respiratory syndrome coronavirus 2 (SARS-CoV-2), often referred to as novel coronavirus disease (COVID-19), was first reported in Wuhan China in early January 2020 [16,17] and on the March 11, 2020, the World Health Organisation (WHO) officially announced COVID-19 as a pandemic [18]. As of the July 30, 2023, WHO reported that over 768 million confirmed cases of COVID-19 infection have been reported globally and over 6.9 million deaths have been documented [19]. It is important to emphasize that the causative agent of COVID-19 respiratory illness is the virus strain SARS-CoV-2 and it is also believed that SARS-CoV-2 originates zoonotically and has close genetic functionality to bat coronaviruses [20].

There are four major structural proteins embedded within the SARS-CoV-2 structure, namely, nucleocapsid (N), membrane (M), envelope (E) and spike (S) proteins [21,22]. M, E and S are embedded on the virus surface envelope while N is embedded inside the virion [23]. S protein undergoes proteolytic cleavage and is categorised as a class I fusion glycoprotein in which two subunits S1 and S2 emerge. For S1 subunit, it hosts the receptor binding domain (RBD) which binds to the angiotensin-converting enzyme II (ACE2) host receptor on cells and then fuses the host and viral membrane via the S2 subunit [24,25]. The basic role of S protein as it relates to viral entry, fusion and attachment to the cells, makes it a primary target for the detection and treatment of SARS-CoV-2 [26], and has been the main target protein used in existing approved COVID-19 vaccines [27].

Accurate (sensitive and selective) and rapid diagnosis of SARS-CoV-2 is necessary to curtail the transmission of COVID-19 among humans. The gold standard test for COVID-19 diagnosis involves nucleic acid amplification tests (NAATs), including loop-mediated isothermal amplification (LAMP), transcription-mediated amplification (TMA) and reverse-transcription real-time polymerase chain reaction (qRT-PCR) [23]. The high cost of analysis, long turnaround time (~1–2 days), laborious sample preparation and sophisticated instrumentation [28–30], associated with these tests, have prompted the need for alternative test methods. Alternative antigen-based methods including lateral flow immunoassays [31], enzyme-linked immuno-sorbent assays [32], electrochemical immunoassays [33] and field-effect transistor assays [34], which detects the absence or presence of the antigens (viral proteins) based on antibody-antigen binding interaction, offers an inexpensive option for SARS-CoV-2 detection. However, low sensitive antigen tests can trigger false negative results for samples containing low viral loads [35,36]. Hence, there is a continual need to develop ultrasensitive diagnostic probes for SARS-CoV-2 with alternative receptors other than antibodies.

To develop a highly efficient MEF biosensor, it is important that both the plasmonic metal NP and nanofluorophore function within a probe system that also embeds an affinity-based receptor. Molecular beacon (MB) represents a type of highly efficient probe system having a hairpin shaped stem-loop oligonucleotide structure where the 5′ end is labelled with a fluorophore and the 3' end is labelled with a quencher [37]. The stem, containing complementary nucleic acid sequences is used to hold the loop, fluorophore and quencher in place so that a hairpin structure is established. The loop on the other hand, contains the nucleic acid sequence that binds to the target analyte. Using a DNA aptamer (Apta) sequence that binds to the RBD of SARS-CoV-2 S protein within a MB probe that embeds a plasmonic NP and a QDs nanocrystal, represents a novel way to develop highly accurate biosensor system for SARS-CoV-2.

This work reports for the first time on the development of an ultrasensitive Apta-MB MEF biosensor for SARS-CoV-2 S protein using newly synthesized silica (SiO_2)–Si-doped ZnSeS QDs with shape and size-controlled cationic cetyltrimethyl ammonium bromide (CTAB)-AuNPs. Si was used as a dopant to alter the QDs electro-optical properties to produce QDs with improved photophysical properties such as high fluorescence QY. To construct the MEF nanobiosensor, COOH–SiO_2–Si-doped ZnSeS QDs were first conjugated to the Apta-MB and cationic CTAB-AuNPs were self-assembled on the QDs-Apta-MB surface. Binding of the target SARS-CoV-2 S protein to the QDs-Apta-MB-AuNPs probe, led to transduction changes on the QDs surface based on the mediation of the QDs fluorescence intensity by LSPR signal from AuNPs. In

addition, we also report on a proof-of-concept study on the application of the Si-doped ZnSeS QDs-Apta-MB probe for the electrochemical detection of SARS-CoV-2 S protein on a carbon nanofiber-modified screen-printed electrode (CNF-SPCE) where the QDs was used as an electroactive signal tag. To the best of our knowledge, this is the first reported MEF and electrochemical biosensor probe for SARS-CoV-2 S protein using a Si-doped ZnSeS QDs QDs-Apta-MB with cationic AuNPs being used to amplify the fluorescence signal.

2. Experimental

2.1. Chemicals and biological materials

Silicon tetrachloride ($SiCl_4$), octadecylphosphonic acid, tetradecylphosphonic acid, trioctylyphosphine oxide (TOPO), dodecanethiol, octadecene, diphenylphosphine, behenic acid, tetramethylammonium hydroxide solution, sodium borohydride, borax, potassium thiocyanate (KSCN), sodium borohydride ($NaBH_4$), CTAB, silver nitrate, (3-aminopropyl)triethoxysilane (APTES), ascorbic acid, sulphur, selenium, trioctylyphosphine (TOP), tris(hydroxymethyl)aminomethane acetate salt (Trizma® Ac), sodium acetate (NaAc), ethylenediaminetetraacetic acid (EDTA) and 3-aminopropyl)triethoxysilane were purchased from Merck. Tetraethyl orthosilicate, gold (III) chloride trihydrate ($HAuCl_4{\cdot}3H_2O$), tetraethyl orthosilicate (TEOS), 2-(*n*-morpholino)ethanesulfonic acid (MES), N-hydroxysuccinimide (NHS), Thermo Scientific™ Pierce™ 1-ethyl-3-(3-dimethylaminopropyl)carbodiimide hydrochloride (EDC) crosslinker, potassium acetate (KAc) and gold (III) chloride trihydrate ($HAuCl_4{\cdot}3H_2O$) were purchased from Thermo Fisher. Tris(hydroxymethyl)aminomethane was purchased from Formedium. SARS-CoV-2 Spike S1-His fusion protein was purchased from InvivoGen. Recombinant influenza A hemagglutinin protein, recombinant dengue virus 1 NS1 protein, recombinant BK polyomavirus, strain AS, major capsid VP1 protein and recombinant human IgG1 protein were purchased from Abcam. SARS-CoV-2 E protein was purchased from the Medical Research Council (MRC) Protein Phosphorylation and Ubiquitylation Unit, University of Dundee. CNF-SPCEs with carbon nanofibers/carbon as the working electrode, carbon as the counter electrode and silver as the reference electrode were purchased from Metrohm. Amino modified anti SARS-CoV-2 Apta-MB with the nucleic acid sequence:

5'-[NH_2C_6]-**GCGAC**CCGCAGGCAGCTGCCATTAGTCTCTATCCGT-GACGGTATG**GTCGC-**[DABCYL]-3′ was synthesized by Eurofins Genomics. The aptamer sequence that binds to the RBD domain of SARS-CoV-2 S protein subunit S1 was adopted from Ref. [38]. DABCYL ([4-((4-(dimethylamino)phenyl)azo)benzoic acid]), a dark quencher, was used as the quencher. The bold sequence in the Apta-MB represents the complimentary stem sequence.

2.2. Equipment

Ultraviolet/visible (UV/vis) absorption and fluorescence emission measurements were performed using a Varian Cary Eclipse spectrophotometer. The settings used for the fluorescence measurements are Excitation and Emission slit = 5 nm; Scan control = medium; Smoothing = moving average with a factor of 99; Excitation filter = Auto; Emission filter = 430–1100 nm and PMT detector voltage = high. Fluorescence polarization analysis was carried out using an Infinite F Flex Multimode plate reader from Tecan. The setting are: Emission bandwidth = 25 nm; Gain = 100; Number of flashes = 25; Integration time = 20 μs; Settle time = 3 ms and G-Factor = 2. Electrochemical measurements were carried out using a Multi Autolab PGSTAT204 potentiostat/galvanostat with Nova 2.1.6 software from Metrohm. Cyclic voltammetry (CV) measurements were carried out in the potential range of 0.7 to −1.0 V in $[Fe(CN)^6]/K^{3-}/^{4-}$; 1.0 to −1.0 V in 0.1 M phosphate buffer and within 0.5 to −0.3 V in $[Fe(CN)^6]/K^{3-}/^{4-}$ buffered with 0.1 M phosphate buffer and $[Fe(CN)^6]/K^{3-}/^{4-}$ buffered with NaAc-KAc-TrizmaAc-KSCN-Borax. Differential pulse voltammetry (DPV) measurements were carried out within the potential range of −1.5 to 0.5 V at an amplitude of 25 mV and deposition potential of −1.2 V. Electrochemical impedance spectroscopy (EIS) measurements were carried out within the frequency range from 100 KHz to 0.1 Hz at an amplitude of 10 mV using the CNF-SPCEs. Transmission electron microscopy (TEM) analysis was carried using a JEOL JEM-1200EX operated at 80 kV. Powder X-ray diffraction (PXRD) analysis was carried out using a Siemens D5000 diffractometer with Cu Kα radiation (λ = 1.54056 nm) and data were obtained in the range of 3–90° using a 0.1° 2θ step size and a 3 s count time per step with a 0.066° slit width. Dynamic light scattering (DLS) was carried out using a Zetasizer Nano ZS series (ZEN3600, Malvern). Energy dispersive X-ray (EDX) analysis was carried out using a JEOL JSM 7400 F field emission scanning electron microscope (SEM) integrated with an Oxford Instruments Inca EDX spectrometer. Fourier transform-infrared (FT-IR) analysis was performed using an Agilent Cary 630 FT-IR spectrometer.

2.3. Preparation of Zn behenate precursor

Zn behenate, used as a precursor for the Si-doped ZnSeS QDs, was synthesized according to literature procedure reported for cadmium benenate but with slight modification [39]. Briefly, 10 g zinc acetate was mixed with 50 mL methanolic solution containing 0.01 g/mL behenic acid, 20 mL chloroform and 5 mL tetramethylammonium hydroxide solution. The solution was stirred under heat for 65 min with the temperature reaching 50 °C. Thereafter, the solution was purified using acetone by ultracentrifugation and the purified zinc behenate was obtained as a white powder.

2.4. Synthesis of blue-emitting Si-doped ZnSeS QDs

Si-doped ZnSeS QDs was synthesized via the organometallic synthetic route for QDs composed of groups II-VI and III-V metal chalcogenides [40]. We emphasize here that the combination of precursor used for the QDs synthesis is the first ever reported in the literature. Briefly, 5 mL $SiCl_4$, 300 mg octadecylphosphonic acid, 500 mg tetradecylphosphonic acid, 3 g TOPO, 10 mL dodecanethiol, 30 mL octadecene and 2 mL diphenylphosphine were mixed in a three-necked flask under nitrogen atmosphere and stirred continuously under intense heat. When the temperature of the reaction solution reached ~260 °C, 3 ml of selenium precursor (prepared by dissolving 0.14 g selenium in 5 mL TOP), zinc behenate solution (prepared by dissolving 0.4 g Zn behenate in 10 mL octadecene) and sulphur precursor (prepared by dissolving 0.18 sulphur in 0.9 g TOPO, 1 mL TOP and 10 mL octadecene) were added. The organic-phased Si-doped ZnSeS QDs were allowed to grow for ~35 min after which the reaction was stopped.

2.5. SiO_2 surface modification of Si-doped ZnSeS QDs

Prior to coating the QDs surface with SiO_2, organic-phased Si-doped ZnSeS QDs were first mixed with chloroform, acetone, ethanol and methanol after which 2 mL $NH_3{\cdot}OH$, 2.5 mL TEOS and 2 mL APTES were added. The solution was stirred vigorously under heat and was stopped after ~30 min at a reaction temperature of ~40 °C. Purification was carried out with acetone via ultracentrifugation to produce powdery NH_2–Si–ZnSeS QDs. To transform the NH_2–Si–ZnSeS QDs to COOH–Si–ZnSeS QDs, 400 mg of NH_2–Si–ZnSeS QDs were mixed with 8 g glutaric anhydride and 100 mL N,*N*-dimethylformamide. The solution was vigorously stirred under heat and stopped after ~30 min at a reaction temperature of ~67 °C. The COOH–Si–ZnSeS QDs were purified using acetone and obtained as a whitish solid product.

2.6. Preparation of shape and size-controlled CTAB-AuNPs

CTAB-AuNPs of different sizes and shapes were prepared via the seed-mediated approach previously reported for shape-controlled AuNPs [41]. The seed solution was traditionally prepared by mixing

5 mL 2.5 × 10^{-3} M $HAuCl_4 \cdot 3H_2O$ with 10 mL CTAB and 0.6 mL ice-cold $NaBH_4$. Different CTAB concentrations of 0.1, 0.2, 0.3 and 0.4 M were prepared and used in the various seed solutions to vary the NP size and shape. Preparation of the growth solution was carried by mixing 5 mL 2.5 × 10^{-3} M $HAuCl_4 \cdot 3H_2O$, with 10 mL CTAB, 500 μL 0.004 M $AgNO_3$ and 400 μL 0.1 M ascorbic acid.

To vary the NP size and shape, different batches of growth solution were prepared as follows: Using 0.1 M CTAB in the seed solution; (i) 300 μL (0.2 M CTAB used in the growth solution), 450 μL (0.3 M CTAB used in the growth solution) and 600 μL (0.4 M CTAB used in the growth solution) seed solution were separately added into the growth solution and left to react; (ii) different seed volumes of 12, 24, 36, 48 and 100 μL (0.1 M CTAB used in the growth solution) were added to the growth solution and left to react (iii) different seed volumes of 24, 48, 72, 96 and 108 μL (0.1 M CTAB used in the growth solution) were added to the growth solution and left to react and (iv) 150 μL of seed solution (0.1 M CTAB used in the growth solution) was added to the growth solution and left to react. To further vary the AuNP size, 24 μL each of the seed solution prepared separately from 0.1, 0.2, 0.3, and 0.4 M CTAB were added into the corresponding growth solution having the same 0.1 M concentration of CTAB. The solutions were left to react for few minutes and thereafter mixed with 30 mL of H_2O.

2.7. Formation of COOH–Si–ZnSeS QDs-Apta-MB conjugate

Conjugation of COOH–Si–ZnSeS QDs to the Apta-MB was carried out using the EDC-NHS carbodiimide coupling chemistry. Briefly, 40 mg of COOH–Si–ZnSeS QD dissolved in 20 mL H_2O was mixed with 1 mL EDC (dissolved in MES buffer pH 5) and stirred for 15 min to activate the COOH group on the QDs surface. Thereafter, 1 mL of 5 pmol/μL Apta-MB (dissolved in Tris-EDTA buffer pH 8) and 1 mL NHS (dissolved in MES buffer pH 5) were added into the reaction solution. The solution was left to react for 45 min under vigorous stirring at ambient temperature. Purification was carried using ethanol via ultracentrifugation.

2.8. MEF bioassay and electrochemical assay

To carry out the MEF bioassay for SARS-CoV-2 S protein, the Si–ZnSeS QDs-Apta-MB probe (1 mg/mL in phosphate buffer pH 7.4) was first electrostatically bonded to CTAB-AuNPs (9.95 × 10^{-11} M) in 1:1 ratio. Thereafter, 175 μL of the formed QDs-AptA-MB-AuNPs was mixed with 200 μL of SARS-CoV-S protein (prepared in PBS buffer pH 7.4) and the fluorescence was measured after ~15 s in a microcuvette. The excitation wavelength was 200 nm and measurement were recorded in the photoluminescence wavelength range of 210–1100 nm.

For the detection of SARS-CoV-S protein, 30 μL of the QDs-Apta-MB probe was drop-casted onto the CNF-SPCE surface and allowed to dry at ambient temperature. Afterward, 15 μL each of SARS-CoV-S protein and the electrolyte solution were dropped on the QDs-Apta-MB-modified CNF-SPCE surface and the corresponding DPV electrochemical signal was recorded.

3. Results and discussion

3.1. TEM analysis

TEM was used to determine the structural morphology of the QDs and AuNPs with respect to their shape and size. For the QDs surface coating, a controlled sol-gel synthetic method was used to establish a homogeneous SiO_2 coating. The encapsulation of the organic-phased QDs in silica particles was carried by a reverse micelle procedure that involved the QDs salination with TEOS in the presence of ammonium hydroxide and APTES, phase transfer from hydrophobic QDs to hydrophilic QDs and SiO_2 shell encapsulation. Fig. 1A shows that the particle morphology of the Si-doped ZnSeS QDs overcoated with SiO_2 shell layer, was a combination of irregularly shaped particles and quasi-spherical shaped particles. The estimated average particle size distribution of ~49 nm demonstrates that the silica coating on the QDs surface influenced the particle morphology. The kinetics of silica coating can be influenced by either the rate of monomer diffusion towards the QDs surface or by the decomposition rate of monomers on the QDs surface.

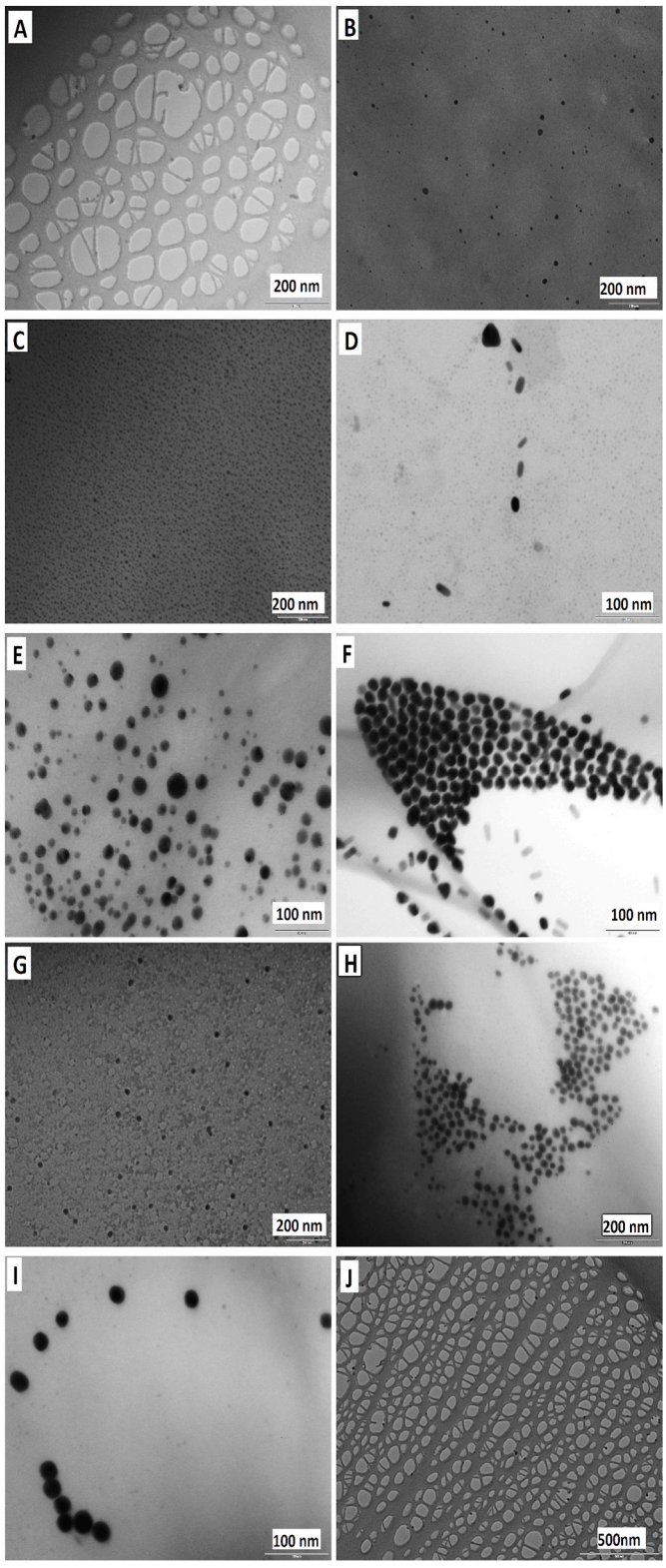

Fig. 1. TEM images of (A) SiO_2–Si-doped ZnSeS QDs and CTAB-AuNPs of size (B) 8 nm, (C) 10 nm, (D) 15 nm, (E) 16 nm, (F) 17 nm, (G) 19 nm, (H) 24 nm, (I) 26 nm and (J) 40 nm.

Since theoretical interpretation predicts that narrow particle size distribution emanates from diffusion-limited growth, it is therefore reasonable to conclude that broadening of the particle size resulted from reaction-controlled silica shell coating [42].

The seed-mediated approach was used to synthesize the cationic AuNPs whilst the amount of seed solution and concentration of CTAB were used to tune the NP size and shape. One of the widely used surfactant in the synthesis of non-spherical AuNPs is CTAB. Theoretical hypothesis suggests that the adsorption of CTA^+-[Br–Ag–Br]- complex ion on the Au crystal {100} facet, allows symmetry breaking to occur, whilst van der Waals interactions holds the alkyl chain together. This process then allows AgBr crystal growth on the Au {100} facet whilst still ensuring CTAB-AgBr electrostatic interactions and aligning Au crystal growth towards the <100> direction. Fig. 1B–J shows the TEM images of the synthesized CTAB-AuNPs of different sizes. The average particle size estimate obtained was 8 nm (Fig. 1B) 10 nm (Fig. 1C), 15 nm (Fig. 1D), 16 nm (Fig. 1E), 17 nm (Fig. 1F), 19 nm (Fig. 1G), 24 nm (Fig. 1H), 26 nm (Fig. 1I) and 40 nm (Fig. 1J). The particle morphology of the 8, 10, 16, 19, 24 and 26 nm sized AuNPs, were mainly characterized by spherical-shaped particles while the 15 and 17 nm sized AuNPs were characterized by a mixture of spherical and rod-shaped particles. The 40 nm sized AuNPs on the other hand was characterized by quasi spherical and irregularly shaped particles.

Fig. 2A shows the TEM images of the QDs-MB conjugate whilst Fig. 2B -J shows the corresponding size-dependent QDs-MB-AuNP nanocomplex. For the QDs-MB conjugate, the particle morphology was like the unconjugated QDs with the shape being predominantly spherical with no sign of particle aggregation. This implies that the MB conjugation did not alter the particle geometry of the QDs, and thus testifies to the strong stability of the QDs. For the size-dependent QDs-MB-AuNP nanocomplex, no visible sign of aggregation was observed in the particle morphology. The shape of the particles was mainly spherical as observed for the unbonded CTAB-AuNPs with the exception that a mixture of rod and spherical-shaped particles were seen in the TEM micrograph of the 17, 24 and 26 nm sized AuNP bonded QDs-MB nanocomplex.

3.2. PXRD analysis

Fig. 3A shows the PXRD pattern of COOH–SiO_2–Si–ZnSeS QDs and the Si–ZnSeS QDs-MB conjugate. The general observation was the similarity in the diffraction pattern of the unconjugated QDs and the QDs-MB conjugate. Both the unconjugated QDs and the QDs-MB conjugate projected a diffraction peak at 22° which corresponds to the diffraction pattern of amorphous silica [43]. The lack of apparent diffraction peaks at >40°, shows the strong effect of Si on the QDs structure. One notable difference in the diffraction pattern was the decrease in intensity in the PXRD pattern of the QDs-MB conjugate relative to the unconjugated QDs. The decrease in intensity may have been induced by the covalent amide bond formation between the QDs and the MB [44].

EDX analysis of the nanomaterial is discussed in the Supplementary Information section (Fig. S1).

3.3. FT-IR analysis

FT-IR analysis was used to characterize the functional groups on the material surface to confirm the material's surface chemistries. Fig. 3B shows the FT-IR spectra of NH_2–SiO_2–Si–ZnSeS QDs, COOH–SiO_2–Si–ZnSeS QDs, Si–ZnSeS QDs-MB and CTAB-AuNPs. For NH_2–SiO_2–Si–ZnSeS QDs, the sharp bands at 2925 cm^{-1} and 2855 cm^{-1} corresponds to the N–H stretching vibration while the bands at 1640 cm^{-1} and 1465 cm^{-1} corresponds to the C═O stretching and C–H bending vibrations, respectively. The bands at 1014 cm^{-1} and 824 cm^{-1} can be ascribed to the SiO and SiO–Si stretching vibrations. For COOH–SiO_2–Si–ZnSeS QDs, there was no visible projection of the sharp N–H stretching vibrations seen in the NH_2–SiO_2–Si–ZnSeS QDs FT-IR spectrum. Rather, a weak and broader band at 3306 cm^{-1} which can be ascribed to the O–H stretching vibration was projected. The absence of the sharp band corresponding to the N–H stretching vibrations, may confirm the surface modification of the NH_2–SiO_2 to COOH–SiO_2.

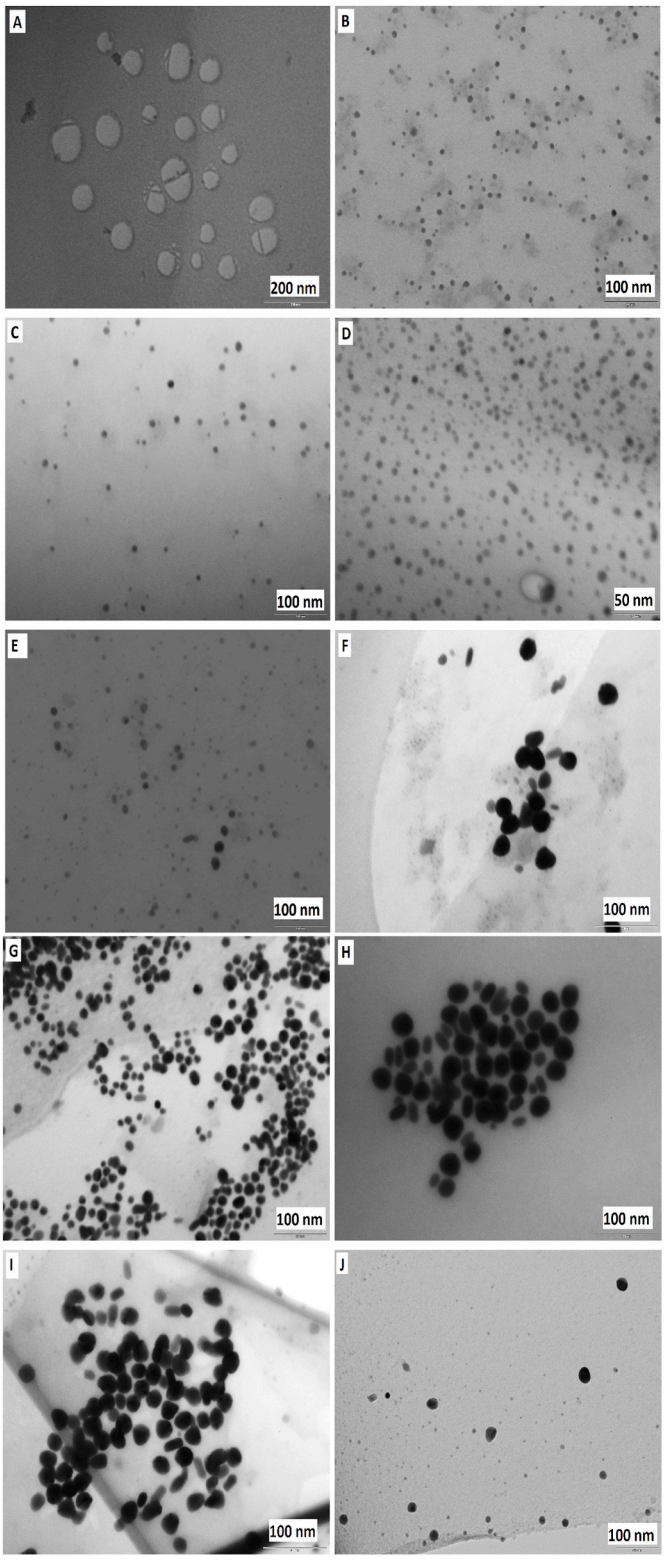

Fig. 2. TEM images of (A) Si-doped ZnSeS QDs-Apta-MB and the Si-doped ZnSeS QDs-Apta-MB-AuNPs conjugate assemble with CTAB-AuNPs of size (B) 8 nm, (C) 10 nm, (D) 15 nm, (E) 16 nm, (F) 17 nm, (G) 19 nm, (H) 24 nm, (I) 26 nm and (J) 40 nm.

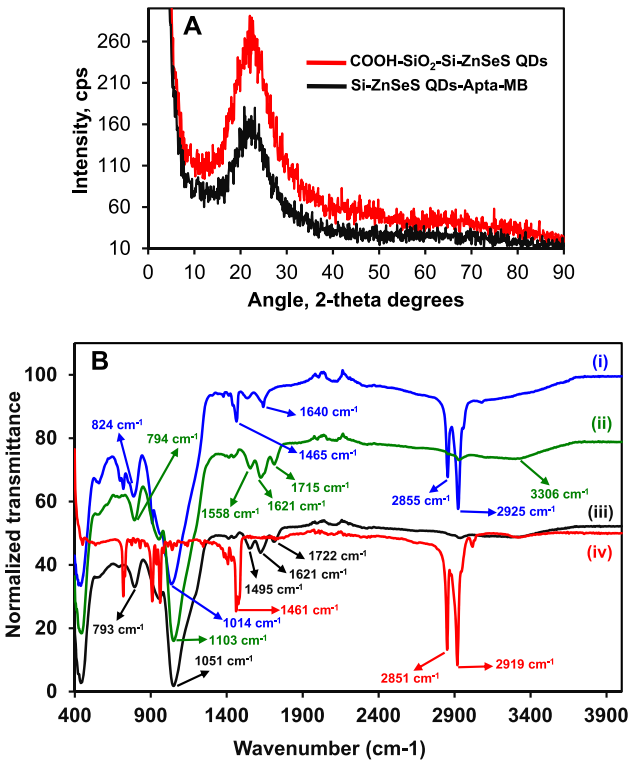

Fig. 3. (A) PXRD pattern for COOH–SiO_2–Si–ZnSeS QDs and Si–ZnSeS QDs-MB. (B) FT-IR spectra of (i) NH_2–SiO_2–Si–ZnSeS QDs, (ii) COOH–SiO_2–Si–ZnSeS QDs, (iii) Si–ZnSeS QDs-MB and (iv) CTAB-AuNPs.

Furthermore, for COOH–SiO_2–Si–ZnSeS QDs, the band at 1715 cm^{-1} corresponds to the C═O stretching vibration while the bands at 1621 cm^{-1} and 1558 cm^{-1} can be ascribed to the N–H bending vibrations. As shown in Scheme 1, COOH–SiO_2 coating on the QDs surface incorporates the N–H functional group within the silica network; hence, the identification by FT-IR confirms the formation of COOH–SiO_2–Si–ZnSeS QDs. With respect to the SiO and SiO–Si stretching vibrations, the shift to higher wavenumber of 1103 cm^{-1} for the SiO band and the shift to lower wavenumber of 794 cm^{-1} for the SiO–Si band, may be used to confirm surface modification changes from NH_2–SiO_2 to COOH–SiO_2.

For CTAB-AuNPs, the sharp bands at 2919 cm^{-1} and 2851 cm^{-1} corresponds to the C–H stretching vibration while the band at 1461 cm^{-1} corresponds to the C–H bending vibration. For the Si–ZnSeS QDs-MB conjugate, the band at 1621 cm^{-1} can be assigned to the CO–NH stretching vibration representing the primary amide bond formation between the QDs and the MB. It is important to emphasize that both the N–H bending vibration of COOH–SiO_2–Si–ZnSeS QDs and the CO–NH stretching vibration of the Si–ZnSeS QDs-MB conjugate were projected at 1621 cm^{-1}. However, the clear difference between the FT-IR spectra was a shift to higher wavenumber of 1722 cm^{-1} of the C═O stretching vibration and a shift to lower wavenumber of 1051 cm^{-1} of the SiO–Si stretching vibration for the Si–ZnSeS QDs-MB conjugate relative to the unconjugated COOH–SiO_2–Si–ZnSeS QDs.

DLS and ZP analysis of the nanomaterials are discussed in the Supplementary Information section (Figs. S2 and S3).

3.4. UV/vis absorption and fluorescence emission

Fig. 4A shows the UV/vis absorption and fluorescence emission spectra of the SiO_2–Si-doped ZnSeS QDs. From the spectra, the QDs exhibited an excitonic absorption peak at 260 nm and fluorescence emission at a wavelength maximum of 490 nm. From the QDs fluorescence emission spectrum, there was no visible sign of peak tailing which is usually associated with deep trap state. This implies that surface defect state in the QDs fluorescence was considerably suppressed. The inset of Fig. 4A shows that the QDs displayed bright blue fluorescence emission under UV light. The fluorescence QY of the QDs was calculated according to equation (1):

$$\Phi_F^{QDs} = \Phi_F^{RHOD} \frac{F_{QDs}.OD_{RHOD(\lambda exc)}.n^2_{water}}{F_{RHOD}.OD_{QDs(\lambda exc)}.n^2_{ethanol}} \quad (1)$$

Φ_F^{QDs} is the representative fluorescence QY of the QDs, Φ_F^{RHOD} is the representative fluorescence QY of rhodamine 6G (Φ = 0.95) and was used as the reference standard [45], F_{QDs} and F_{RHOD} are the integrated sum of the fluorescence intensity of the QDs and rhodamine standard, $OD_{RHO(\lambda exc)}$ and $OD_{QDs(\lambda exc)}$ are the optical densities of rhodamine 6G and the QDs, while the refractive index of water and ethanol are denoted by n^2_{water} and $n^2_{ethanol}$ respectively. The calculated fluorescence QY of the synthesized Si-doped ZnSeS QDs was 88%. This strongly indicates that surface defect state in the QDs was suppressed to very high degree, a characteristic that is uncommon for cadmium-free QDs.

Fig. 4B shows that the Apta-MB binding on the QDs quenched the QDs fluorescence and with cationic AuNPs assembly on the QDs-Apta-MB probe, the QDs fluorescence was slightly enhanced. Using the QDs-Apta-MB (without cationic AuNP) to detect SARS-CoV-2, the fluorescence enhancement signal was minimal but when the QDs-Apta-MB-AuNP probe was used to detect SARS-CoV-2, the fluorescence emission signal was greatly enhanced. This proves to show that the assembled AuNP, amplified the fluorescence intensity signal of the QDs based on LSPR mediated effect.

The representative solution colour and UV/vis absorption spectra of the different-sized positively charged CTAB-AuNPs is shown in Fig. 4C and D. As outlined in Section 2.6, the amount of seed solution and concentration of CTAB were used to tune the shape and size of the AuNPs. TEM analysis showed that the morphology of the NPs was either fully spherical or a blend of spherical and rod-shaped particles. ZP analysis on the other hand confirmed that all the AuNPs synthesized in this work were positively charged (Figs. S2 and S3). The absorption spectra of the NPs were characterized by strong transverse absorption peaks in the UV/vis region which is indicative of spherical-shaped AuNP absorption and a much weaker longitudinal absorption peak in the near infra-red region that is indicative of rod-shaped AuNP absorption. Table 1 shows the summary of the transverse and longitudinal absorption wavelength of the different-sized CTAB-AuNPs.

3.5. Fluorescence polarization (FP)

FP is a technique that is based on the principle that when polarized light excites a fluorophore, light is emitted with a degree of polarization that translates inversely to the level of molecular rotation [46]. Thus, FP represents a viable technique for characterizing, for example, protein-protein and nucleic acid-protein interactions where the molecular weight of the bound protein determines the degree of molecular rotation, i.e., higher molecular weight protein binding = lower FP and vice versa. In this work, FP was used as a technique to study the QDs binding to the MB surface and the QDs-Apta-MB-AuNP binding to SARS-CoV-2 S protein. From Fig. 5A, the FP signal for the unbound QDs was high but when the Apta-MB was conjugated to the QDs, the FP signal deceased by 0.049 mP, implying the QDs felt the molecular weight of the MB. Upon binding of the QDs-Apta-MB to AuNPs, the FP signal further decreased by 0.077 mP whilst binding of SARS-CoV-2 S protein to the QDs-Apta-MB-AuNP further decreased the FP signal by 0.076 mP. To confirm that the FP signal obtained was due to the different binding processes, the QDs when mixed with the Apta-MB produced a FP signal that was higher than that of the QDs-Apta-MB conjugate, thus, indicating that the QDs did not feel the molecular

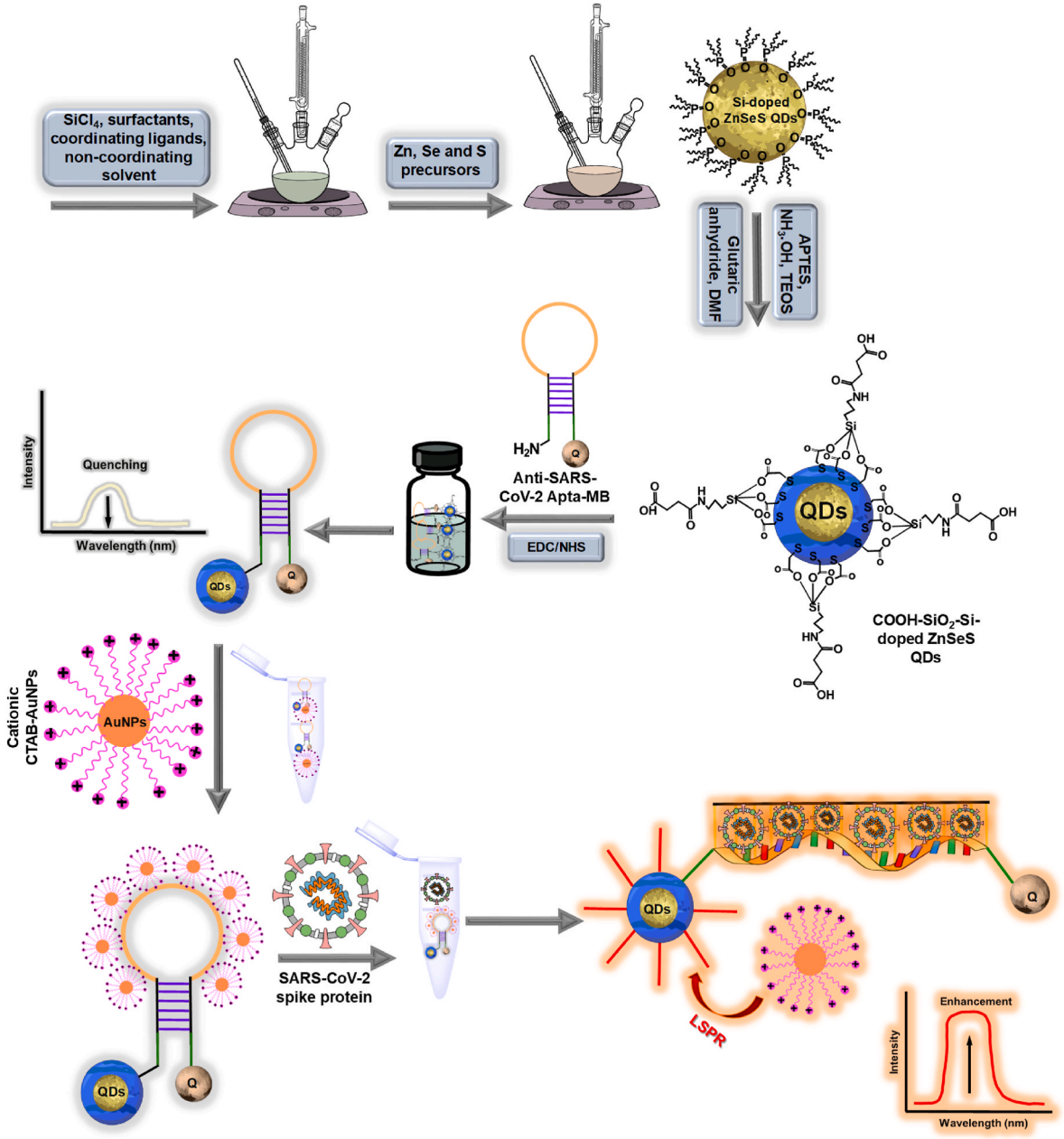

Scheme 1. Schematic description of the Si–ZnSeS QDs-Apta-MB-AuNP MEF biosensor probe for SARS-CoV-2 S protein. Organic-phased Si-doped ZnSeS QDs were synthesized and capped with SiO_2. SiO_2–Si–ZnSeS QDs was then conjugated to the anti-SARS-CoV-2 Apta-MB to form a Si–ZnSeS QDs-Apta-MB probe. Cationic CTAB-AuNPs are immobilized on the Si–ZnSeS QDs-Apta-MB probe, forming an electrostatic interaction with the negatively charged nucleic acid sequence. Upon interaction of SARS-CoV-2 S protein, the electrostatic interaction between the nucleic acid sequence and cationic AuNPs is broken and the aptamer folds to bind the target SARS-CoV-2 S protein. This in turn leads to an increase in the distance between the Si–ZnSeS QDs and the quencher and LSPR signal from AuNPs mediates the fluorescence intensity signal leading to the development of a MEF biosensor for SARS-CoV-2 S protein.

weight of the Apta-MB, hence higher FP signal. However, the significant decrease in FP signal by 0.152 mP of the QDs-Apta-MB (mixed)-AuNPs relative to the QDs-MB (mixed), may suggest that since the Apta-MB and the QDs flowed freely in solution, AuNPs electrostatically bonded to both the QDs and Apta-MB and this influenced the very low FP signal observed when SARS-CoV-2 S protein was added into the mixed system. The result thus confirmed the conjugation of the QDs to the MB, QDs-MB binding to AuNPs and subsequent recognition of SARS-CoV-2 S protein by the QDs-Apta-MB-AuNP probe.

3.6. Assay optimization

Assay optimization was carried out to determine the precise analytical parameters to use for the biosensor assay with the aim of ensuring a highly sensitive and selective nanoprobe is developed for SARS-CoV-2 S protein. The effects of AuNP size, ratio of QDs-Apta-MB to AuNP (v/v) (QDs-Apta-MB volume kept constant and AuNP volume varied), pH and QDs-Apta-MB concentration on the fluorescence detection of SARS-CoV-2 S protein was studied. Fig. 5B shows the fluorescence signal response for the effect of AuNP size on the fluorescence detection of SARS-CoV-2 using the QDs-Apta-MB to AuNP MEF probe. Nine cationic CTAB-AuNPs were tested and from the data obtained, the strongest fluorescence intensity signal was obtained upon using the 40 nm-sized CTAB-AuNPs in the QDs-Apta-MB probe system. In addition, tests were carried out to investigate the conductivity of the tested AuNP sizes. The conductivity data shown in Fig. S4, clearly

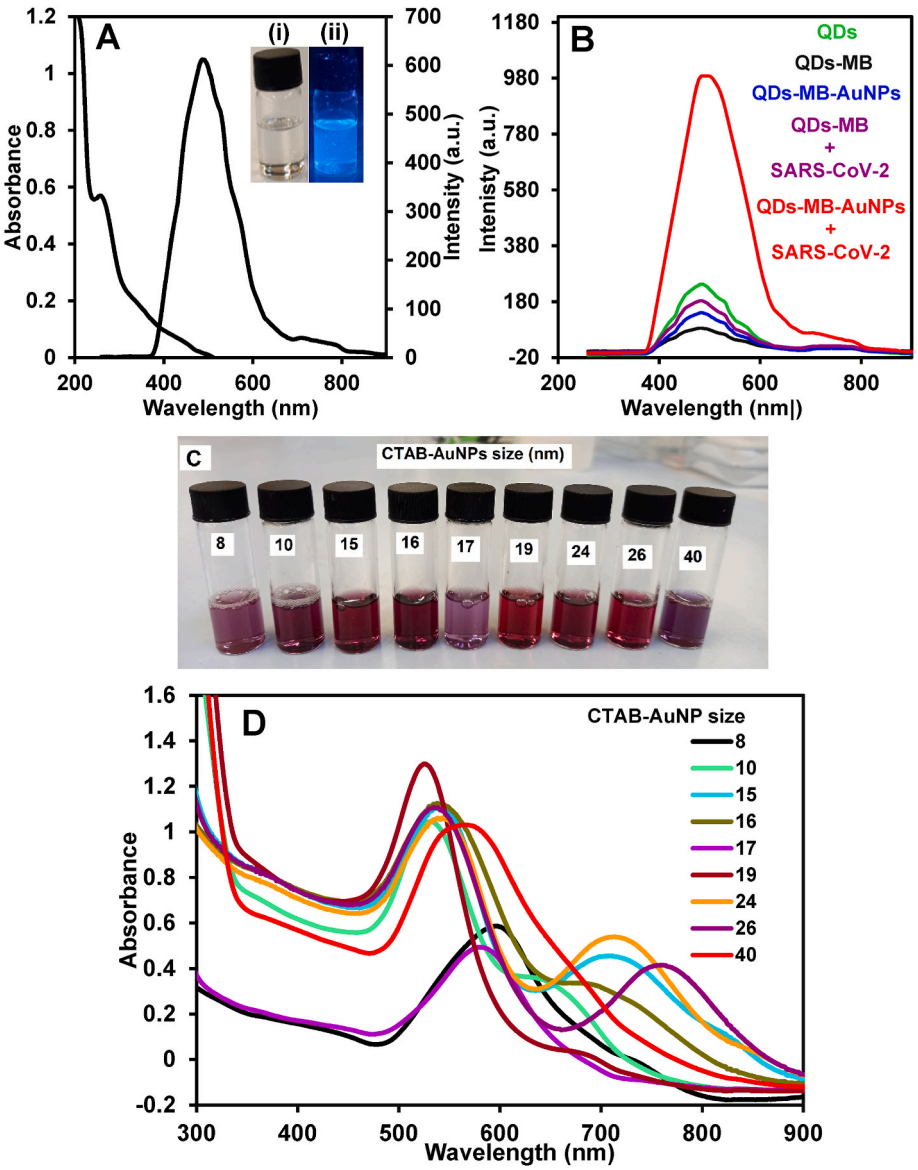

Fig. 4. (A) UV–vis absorption and fluorescence emission spectra of the SiO_2–Si-doped ZnSeS QDs. (B) Fluorescence emission spectra of the unconjugated SiO_2–Si-doped QDs (green), Si–ZnSeS QDs-MB conjugate (black), QDs-Apta-MB-AuNPs (blue), QDs-MB + SARS-CoV-2 (purple) and QDs-Apta-MB-AuNPs + SARS-CoV-2 (red). (C) Photographic pictures of the different sized CTAB-AuNPs. (D) UV/vis absorption spectra of the different sized CTAB-AuNPs. Inset of Fig. 1A: Photograph of the QDs solution in ambient light (i) and under UV light (ii). (For interpretation of the references to colour in this figure legend, the reader is referred to the Web version of this article.)

Table 1
Analytical parameters for the detection of SARS-CoV-2 S protein in saliva using the developed QDs-Apta-MB-AuNP MEF biosensor probe.

Matrix	SARS-CoV-2 added, pg/mL	Found (pg/mL)	Recovery (%)	RSD (%, n = 3)
Saliva	10	10.1	101.0	4.0
	0.4	~0.4	99.5	2.8
	0.016	0.016	100.1	11.2

revealed that the conductivity of the tested AuNPs sizes did not follow a symmetric size trend as each AuNP conductivity was unique to its size. Thus, it can be argued that the effects of AuNP size on the fluorescence intensity signal for SARS-CoV-2 detection, did not follow a size-dependent trend, but rather the fluorescence intensity signal was specific to each AuNP size. Based on the obtained results, the 40 nm-sized CTAB-AuNPs was further used in the fluorescence bioassay. The UV/vis absorption spectra displayed in Fig. S5A, showed that for each tested AuNP size, the transverse and longitudinal absorption peaks were retained but with degrees of shift and absorbance strength as compared to the UV/vis spectra of the AuNPs in their unbonded state as shown earlier in Fig. 4D. In general, the UV/vis absorption study confirmed that the geometry of the tested AuNP size was not distorted in the probe system, thus, giving credibility to the obtained fluorescence signal.

The fluorescence intensity signal obtained for SARS-CoV-2 upon studying the effect of the QDs-Apta-MB ratio to the 40 nm-sized AuNP (v/v) (with the QDs-Apta-MB volume being kept constant and that of AuNP volume varied), showed that at QDs-Apta-MB to AuNP (v/v) 1:1 ratio, the strongest fluorescence signal was obtained (Fig. 5C). Hence, based on the obtained result, QDs-Apta-MB to AuNP (v/v) 1:1 ratio was chosen as the optimal ratio for the fluorescence assay. The measured UV/vis absorption spectra displayed in Fig. S5B, showed that the SPR absorption peak for the 40 nm-sized AuNPs increased as the volume amount of AuNP increased in the QDs-Apta-MB probe system. Thus, the

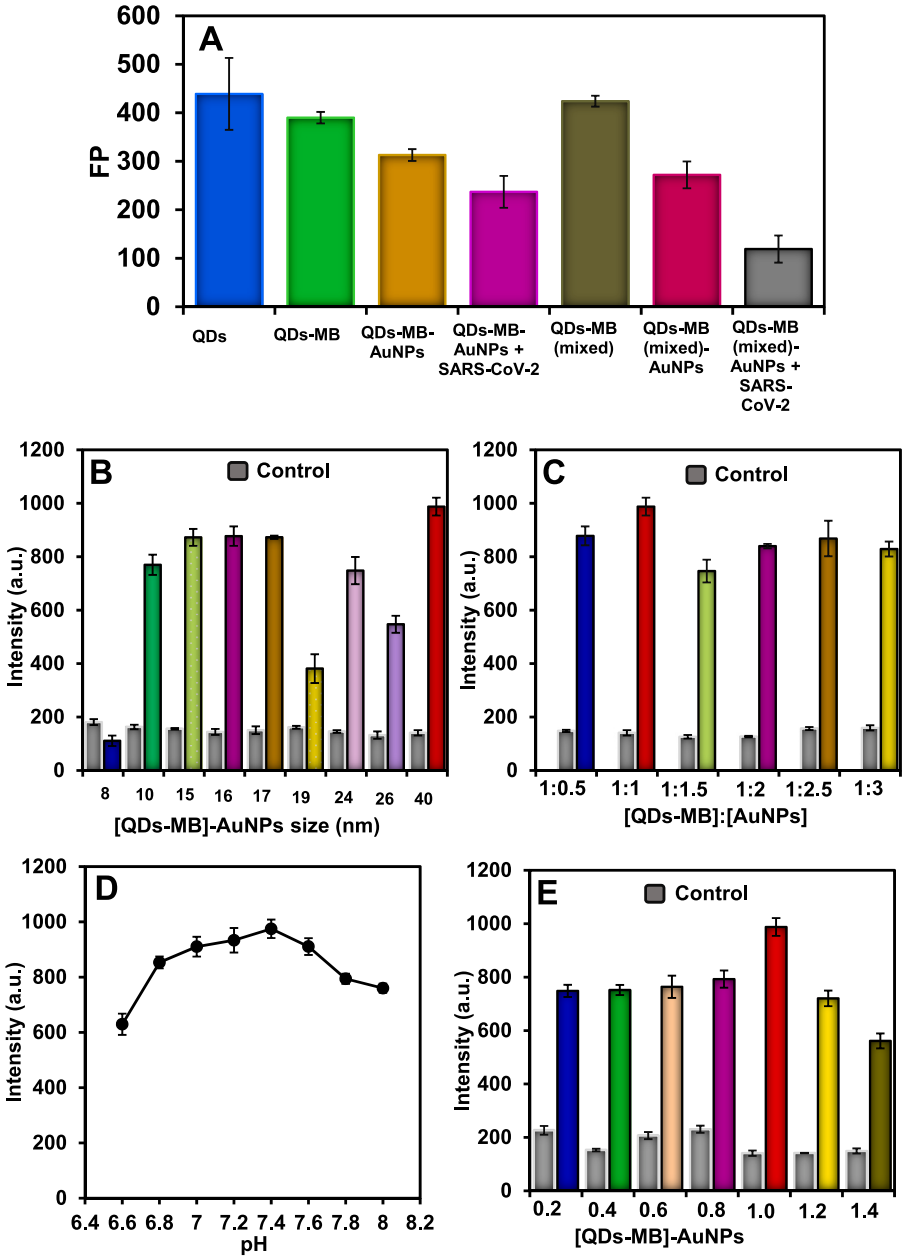

Fig. 5. (A) FP data to confirm binding of the SARS-CoV-2 to the QDs-Apta-MB-AuNP conjugate probe. Fluorescence intensity signal generated for SARS-CoV-2 S protein detection from studying the effects of (B) AuNPs size on the QDs-Apta-MB-AuNP probe, (C) ratio of QDs-MB to AuNPs (v/v) at a fixed QDs-MB volume and varied AuNPs volume, (D) pH, and (E) QDs-MB concentration at a fixed AuNPs concentration. [SARS-CoV-2 S protein] = 10 pg/mL. FP of Fig. 5A = Fluorescence polarization.

results also indicate that the geometry of the tested AuNP was not distorted in the QDs-Apta-MB probe system.

The effect of pH on the fluorescence detection of SARS-CoV-2 using the QDs-Apta-MB probe shown in Fig. 5D, revealed a steady increase in fluorescence intensity signal as the pH increased and reached a maximum at pH 7.4 and decreased steadily afterward. Based on the obtained result, pH 7.4 was chosen as the optimal pH for the fluorescence assay.

The effect of the QDs-Apta-MB concentration on the fluorescence detection of SARS-CoV-2 using the QDs-Apta-MB-AuNP probe was also investigated. Fig. 5E showed that the strongest fluorescence intensity signal was obtained with 1 mg/mL QDs-Apta-MB concentration in the probes system. Hence, based on the obtained result, 1 mg/mL QDs-Apta-MB concentration was used for the fluorescence assay.

3.7. Electrochemical characterization

3.7.1. CV

Electrochemical characterization of the QDs, MB and the QDs-Apta-MB conjugate was carried out in different electrolyte solution using CV. For this study, AuNPs was not incorporated into the probe system as it played no important role in the electrochemical process, i.e., electron transfer processes were poor with AuNPs in the system. Fig. 6A–D shows the CV plots of the QDs, MB and the QDs-Apta-MB conjugate in [$Fe(CN)_6$]/K^{3-}/$^{4-}$ (Fig. 6A), 0.1 M phosphate buffer (Fig. 6B), [$Fe(CN)_6$]/K^{3-}/$^{4-}$ buffered with 0.1 M phosphate buffer (Fig. 6C) and [$Fe(CN)_6$]/K^{3-}/$^{4-}$ buffered with NaAc-KAc-TrizmaAc-KSCN-Borax (Fig. 6D). For all the electrolyte solution, 0.1 M KCl was used as a supporting electrolyte. From Fig. 6A, well-defined oxidation (E_{pa} = 159 mV ± 1.4) and

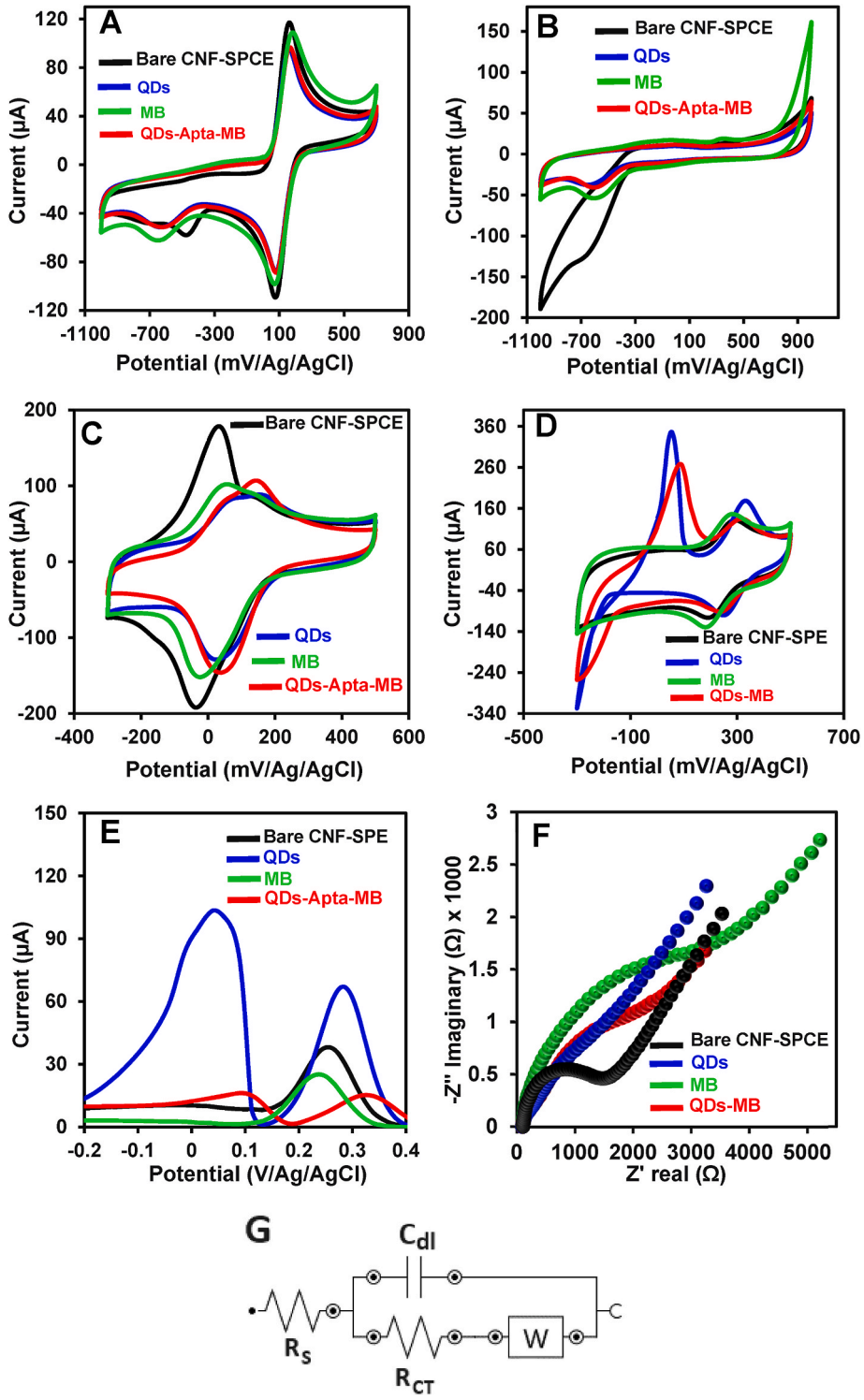

Fig. 6. CV of bare CNF-SPCE, QDs, MB and the QDs-Apta-MB conjugate in (A) $[Fe(CN)_6]/K^{3-/4-}$, (B) 0.1 M phosphate buffer (C) $[Fe(CN)_6]/K^{3-/4-}$ buffered with 0.1 M phosphate buffer and (D) $[Fe(CN)_6]/K^{3-/4-}$ buffered with NaAc-KAc-TrizmaAc-KSCN-Borax. 0.1 M KCl was used as a supporting electrolyte. Concentration of the QDs and QDs-MB were kept constant at 1 mg/mL whilst the concentration of MB was kept constant at 5 pmol/μL throughout the CV measurements. (E) DPV and (F) EIS Nyquist plots of bare CNF-SPCE, QDs, MB and the QDs-Apta-MB conjugate measured in $[Fe(CN)_6]/K^{3-/4-}$ buffered with NaAc-KAc-TrizmaAc-KSCN-Borax with 0.1 M KCl. (G) Randle's equivalent circuit for EIS plots of Fig. 6F.

reduction (E_{pc} = 78 mV ± 0) peaks were observed for the bare CNF-SPCE in $[Fe(CN)_6]/K^{3-/4-}$ with the half wave potential being $E_{1/2}$ = 120 mV ± 0.7. Notable feature was the decrease in anodic peak current for the unconjugated QDs which may have been induced from the conductive nature of the QDs. The anodic peak current for the MB decreased slightly relative to the QDs whilst that of the QDs-Apta-MB increased slightly relative to the unconjugated QDs. No notable changes in $E_{1/2}$ were observed for the materials relative to the bare CNF-SPCE.

In 0.1 M phosphate buffer (Fig. 6B), a weak and broad reduction peak was observed around −700 to −550 mV for the bare CNF-SPCE whilst the CV of the QDs, MB and the QDs-Apta-MB conjugate did not show any

major change with the exception that the cathodic peak current decreased relative to the bare CNF-SPCE. In $[Fe(CN)_6]/K^{3-}/^{4-}$ buffered with 0.1 M phosphate buffer (Fig. 6C), the bare CNF-SPCE exhibited a $E_{1/2}$ of 33 mV ± 0 which was much smaller than what was observed in $[Fe(CN)_6]/K^{3-}/^{4-}$ (without phosphate buffer). Corresponding $E_{1/2}$ for the QDs and QDs-Apta-MB was 89 mV ± 0.7 whilst that of the MB was 38 mV ± 1.9. The $E_{1/2}$ values generally implies that the electrochemical process was reversible. Other notable features were the reduction in peak current and shift to higher potential for the QDs at the anodic sweep relative to the bare CNF-SPCE and the slight increase in anodic peak current for the QDs-Apta-MB relative to the QDs. For CV measurements in $[Fe(CN)_6]/K^{3-}/^{4-}$ buffered with NaAc-KAc-TrizmaAc-KSCN-Borax (Fig. 6D), the bare CNF-SPCE displayed characteristic oxidation and reduction peaks that corresponds to the redox probe ($[Fe(CN)_6]/K^{3-}/^{4-}$); however for the QDs CV, a new oxidation peak at 54 mV ± 1.4 with high peak current was observed that was not seen in the bare CNF-SPCE CV. Also, the anodic peak potential of the QDs corresponding to the redox probe was projected at higher peak current relative to the bare CNF-SPCE. This proves to show that the QDs induced higher electron transfer rates in the $[Fe(CN)_6]/K^{3-}/^{4-}$ buffered with NaAc-KAc-TrizmaAc-KSCN-Borax redox probe. For the CV of MB, there was no presence of the new oxidation peak observed for CV of the QDs which strongly implies that the new anodic peak corresponds specifically to the QDs. For the QDs-Apta-MB, the new oxidation peak was projected alongside the oxidation and reduction peaks of the redox probe. Also, the new anodic peak current specific for the QDs, decreased in the QDs-Apta-MB CV relative to the unconjugated QDs and may be attributed to the MB binding to the QDs surface.

3.7.2. DPV

DPV of the QDs, MB and the QDs-Apta-MB conjugate were studied in the four-electrolyte solution used to characterize the CV of the bioprobe system. Fig. S6 shows the DPV of the QDs, MB and the QDs-Apta-MB conjugate in $[Fe(CN)_6]/K^{3-}/^{4-}$ (Fig. S6A), 0.1 M phosphate buffer (Fig. S6B) and $[Fe(CN)_6]/K^{3-}/^{4-}$ buffered with 0.1 M phosphate buffer (Fig. S6C). In $[Fe(CN)_6]/K^{3-}/^{4-}$, decrease in the anodic peak current was observed for the QDs, MB and the QDs-Apta-MB conjugate relative to the bare CNF-SPCE. However, in 0.1 M phosphate buffer, the anodic peak current for the QDs increased relative to the bare CNF-SPCE and was much lower for the MB but increased significantly for the QDs-MB. Although, the anodic peak current for the QDs-Apta-MB conjugate was significantly high in $[Fe(CN)_6]/K^{3-}/^{4-}$ buffered with 0.1 M phosphate buffer, the peak current for the QDs was lower than the bare CNF-SPCE whilst the peak current for the MB was higher than for the QDs and bare CNF-SPCE but lower than the QDs-Apta-MB conjugate. In $[Fe(CN)_6]/K^{3-}/^{4-}$ buffered with NaAc-KAc-TrizmaAc-KSCN-Borax (Fig. 6E), the bare CNF-SPCE displayed a single anodic peak which can be attributed to the redox probe. However, the DPV of the QDs showed two anodic peaks, with one around 290 mV that corresponds to the redox probe and the other around 50 mV that evidently corresponds to the QDs. Since the MB DPV did not display the new anodic peak, it is justifiable to attribute the new anodic peak to the QDs. The presence of the two anodic peaks in the QDs-Apta-MB DPV, further confirms that the new anodic peak corresponds to the QDs. The decrease in current for the two anodic peaks (QDs + redox probe) for the QDs-Apta-MB relative to the QDs, can be attributed to the MB binding to the QDs. $[Fe(CN)_6]/K^{3-}/^{4-}$ buffered with NaAc-KAc-TrizmaAc-KSCN-Borax, thus, represent a viable electrolyte solution to be used for the detection of SARS-CoV-2 using the QDs-Apta-MB probe.

3.7.3. EIS

EIS Nyquist plots for the QDs, MB and the QDs-Apta-MB conjugate were studied in the four-electrolyte solutions used for CV and DPV characterization. Fig. 6F shows the EIS Nyquist plots for the QDs, MB and the QDs-Apta-MB conjugate measured in $[Fe(CN)_6]/K^{3-}/^{4-}$ buffered with NaAc-KAc-TrizmaAc-KSCN-Borax. The plots consisted of a straight line that transcends along the low frequency region, whilst for the high frequency region, a characteristic strong semicircle was observed for the bare CNF-SPCE but weakened and broadened for the QDs and QDs-Apta-MB conjugate. The Randle's equivalent circuit used to fit the EIS plots is shown in Fig. 6G. The solution resistance (R_S) for the QDs was 98.9 Ω ± 0.6 while that for the QDs-Apta-MB was ~99.0 Ω ± 0.4; the charge transfer resistance (R_{CT}) was 225.2 Ω ± 7.6 for the QDs and 328.9 Ω ± 0.6 for the QDs-Apta-MB. The lower R_{CT} value for the QDs relative to the QDs-Apta-MB, suggest that during the charging-discharging process, there was faster conduction of ions. The presence of the Warburg resistance (Z_W) gives indication of the ion diffusion occurrence at the electrode-electrolyte interface. Data and discussion on the EIS Nyquist plots of the individual biosensor component in the other studied electrolyte solution is provided in the Supplementary Information section (Fig. S7).

3.8. Selectivity

The selectivity of the QDs-Apta-MB-AuNP fluorescent probe and the QDs-Apta-MB electrochemical probe for SARS-CoV-2 S protein detection was studied in the presence of other viral proteins including SARS-CoV-2 E protein, BK polymavirus protein, influenza virus protein and dengue virus protein. Fig. 7A shows the fluorescence intensity signal for SARS-CoV-2 S protein detection in comparison to other tested viral proteins. The results showed that the fluorescence signal for SARS-CoV-2 S protein was at most 2-fold higher than the signal obtained for the tested viral proteins, thus, confirming that SARS-CoV-2 S protein bonded selectively to the Apta-MB with the QDs transducing the signal and AuNPs amplifying the signal. For the electrochemical selectivity studies,

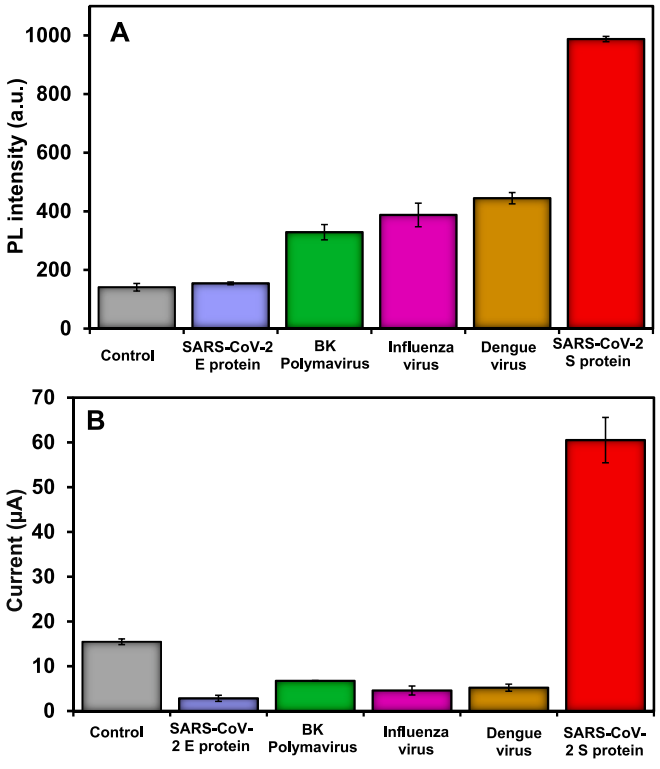

Fig. 7. (A) Fluorescence intensity signal for SARS-CoV-2 S protein detection in comparison to other viral proteins using the QDs-Apta-MB-AuNPs fluorescent biosensor probe. (B) DPV current signal for SARS-CoV-2 S protein detection in comparison to other viral proteins using the QDs-Apta-MB electrochemical biosensor probe. For Fig. 7A, all tested viral protein concentration was 10 pg/mL and control = QDs-Apta-MB-AuNPs. For Fig. 7B, all tested viral protein concentration was 2 pg/mL and control = QDs-Apta-MB.

Fig. 7B shows the DPV anodic current signal obtained for SARS-CoV-2 S protein in comparison to the other tested viral proteins. The results showed clearly that the anodic current for SARS-CoV-2 S protein was far superior to the current obtained for the other tested viral proteins which is indicative of a selective transfer of electron from the analyte solution to the electrode surface because of SARS-CoV-2 S protein binding to the QDs-Apta-MB probe. More importantly, both the QDs-Apta-MB-AuNP fluorescent probe and the QDs-Apta-MB electrochemical probe were able to selectively distinguish SARS-CoV-2 S protein from SARS-CoV-2 E protein based on the superior detection signal obtained for the former.

3.9. Reaction mechanism

Scheme 1 shows the schematic description of the reaction mechanism for SARS-CoV-2 S protein detection using the Si–ZnSeS QDs-Apta-MB-AuNP MEF biosensor probe. After coating the surface of the QDs with COOH-silica, COOH–SiO_2–Si–ZnSeS QDs were conjugated to the Apta-MB via EDC/NHS chemistry. The conjugation then led to non-radiative recombination exciton (electron and hole) process where the fluorescence of the QDs was quenched. Cationic CTAB-AuNPs were self-assembled on the QDs-Apta-MB, where electrostatic interaction was established with the negatively charged nucleic acids. Nucleic acids are known to be highly negatively charged as reported in the literature [47]. Hence, with no available negative charge on the QDs surface or the dark quencher attached to the MB, it is reasonable to say that the cationic CTAB-AuNPs bonded to the nucleic acids that formed the loop structure of the MB. Prior to the detection of SARS-CoV-2 S protein, the QDs-Apta-MB-AuNP probe maintained a hairpin stem-loop structure with the QDs, and the quencher being separated by a short distance. However, upon interaction of SARS-CoV-2 S protein with the QDs-Apta-MB-AuNP probe, cationic AuNPs was detached, the aptamer then folds to bind the viral protein and the distance been the QDs and quencher becomes longer due to the hairpin stem-loop structure being distorted. LSPR signal from the detached cationic AuNPs then amplifies the transduced fluorescence intensity signal from the QDs, leading to MEF detection for SARS-CoV-2 S protein. Thus, the electron and hole recombination process of the QDs is reactivated leading to a radiative fluorescence emission process.

Scheme 2 shows the descriptive electrochemical detection strategy for SARS-CoV-2 S protein using the QDs-Apta-MB probe. Firstly, it is important to note that with semiconductor materials, quasi-continuum bands are formed from electronic energetic levels which implies that the electronic levels divide into valence and conduction bands. Thus, the energy difference between the lowest unoccupied molecular orbital (LUMO) and the highest occupied molecular orbital (HOMO) is determined by the QDs particle size. The energy gap generated between the LUMO and HOMO is then electrochemically detected [48]. Upon conjugation of the QDs to the Apta-MB, the DPV peak current of the QDs-Apta-MB decreased relative to the QDs which clearly points to the Apta-MB binding effect on the QDs. However, in the presence of SARS-CoV-2 S protein, the aptamer fold to bind the target viral protein and this led to increase in the anodic peak current. It is thus important to emphasize that the anodic peak current observed for the DPV plot, implies that the electrochemical oxidation process involved transfer of electrons from the Fermi level of the QDs valence band to the electrode surface as shown in Scheme 2.

3.10. Quantitative detection

Quantitative detection of SARS-CoV-2 S protein in the concentration range of 10 pg/mL to 0.0032 pg/mL (3.2 fg/mL) was carried using the QDs-Apta-MB-AuNP MEF biosensor probe. Fig. 8A shows that as the concentration of SARS-CoV-2 S protein increased in the system, the fluorescence emission spectra of the bound QDs were enhanced. There was no significant peak shift in the fluorescence emission spectra of the bound QDs for each detected SARS-CoV-2 S protein concentration which proves to show that the QDs fluorescence was stable within the detected concentration range. A linear calibration plot detailing the plot of the fluorescence intensity signal versus SARS-CoV-2 S protein concentration is shown in Fig. 8B. The limit of detection (LOD) was calculated using LOD = 3 δ/K, where δ denotes standard deviation of blank measurements (n = 10) and K denoting the slope of the linear calibration plot.

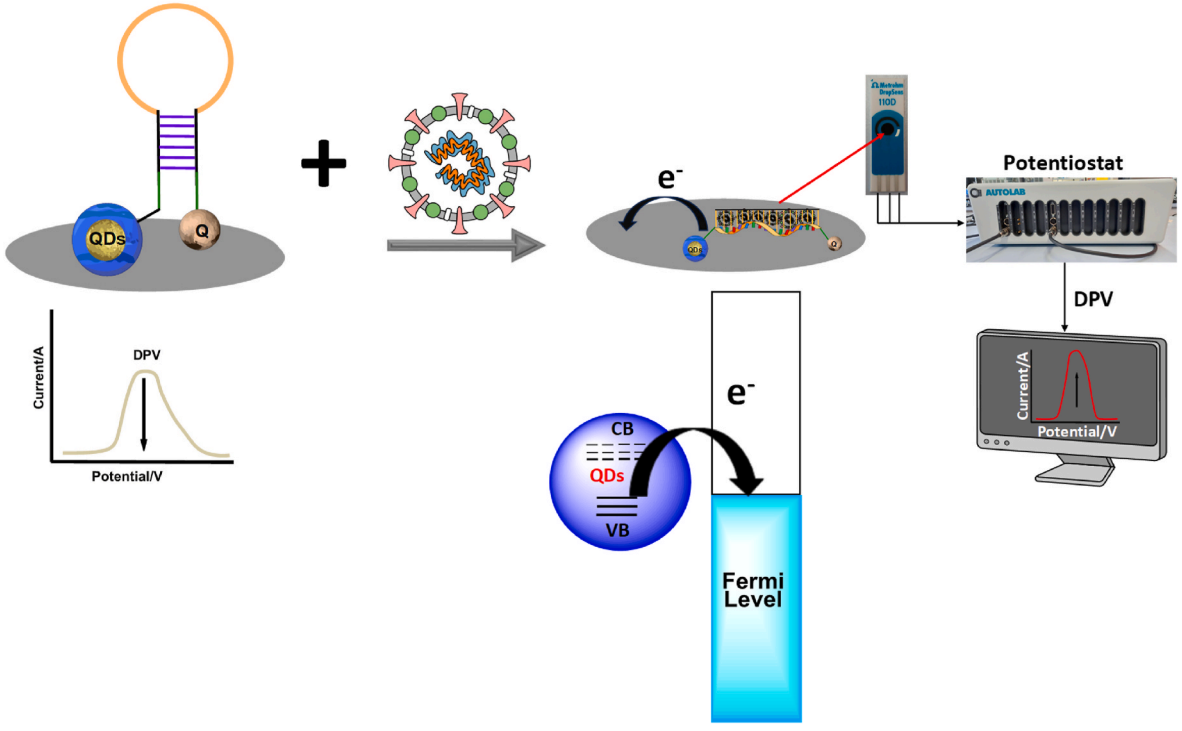

Scheme 2. Schematic description of the QDs-Apta-MB probe for the electrochemical detection SARS-CoV-2 S protein and the electron transfer process from the Fermi level of the QDs valence band (VB) to the electrode surface. CB = conduction band.

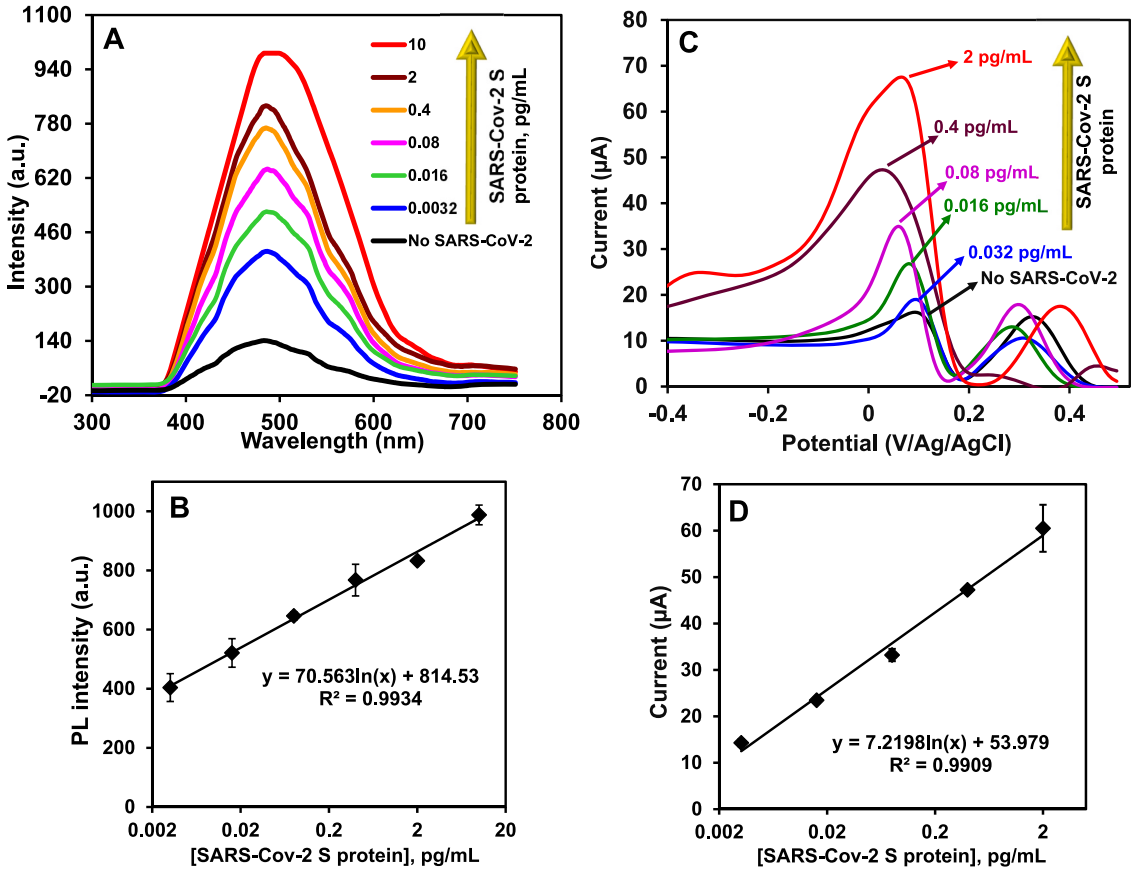

Fig. 8. Fluorescence emission spectra (A) and corresponding fluorescence intensity calibration plot (B) obtained for the quantitative detection of SARS-CoV-2 S protein using the QDs-Apta-MB-AuNPs biosensor probe. (C) DPV plots for SARS-CoV-2 S protein quantitative detection and (D) corresponding calibration plot using the QDs-Apta-MB probe.

From the linear calibration plot, the limit of detection (LOD) for SARS-CoV-2 S protein using the QDs-Apta-MB-AuNP MEF probe was determined as 0.0089 pg/mL (8.9 fg/mL).

For the electrochemical detection, Fig. 8C shows the DPV plots for the quantitative detection of SARS-CoV-2 S protein in the concentration range of 2 pg/mL to 0.0032 pg/mL (3.2 fg/mL) using the QDs-Apta-MB probe. As the concentration of SARS-CoV-2 S protein increased in the system, the anodic peak current specific for the QDs increased progressively with the anodic peak of the redox probe being unresponsive. Such response points to the fact that SARS-CoV-2 S protein successfully bonded to the Apta-MB with the bound QDs transducing the electrochemical signal. The corresponding calibration plot followed a linear regression as shown in Fig. 8D and the calculated LOD (3 δ/K) for SARS-CoV-2 S protein using the QDs-Apta-MB electrochemical probe was ~0.5 pg/mL.

Table S2 shows the comparison of the analytical parameter of the QDs-Apta-MB-AuNP MEF and the QDs-Apta-MB electrochemical probe for the detection of SARS-CoV-2 S protein in comparison to other published. The data comparison showed that our system offered improved sensitivity.

3.11. Detection in saliva

To validate the efficacy of the developed probe to detect SARS-CoV-2 S protein in real samples, detection of SARS-CoV-2 S protein in saliva was carried out using the QDs-Apta-MB-AuNP MEF probe. Saliva samples were ethically collected and used without pre-treatment. Table 1 shows the analytical performance of the QDs-Apta-MB-AuNP MEF probe for the detection of 10, 0.4 and 0.016 pg/mL concentrations of SARS-CoV-2 S protein spiked in saliva. The result showed an excellent recovery rate which is indicative of the accuracy of the probe to detection SARS-CoV-2 S protein in complex samples.

4. Conclusion

We have successfully developed a novel QDs-Apta-MB-AuNP MEF and QDs-Apta-MB electrochemical biosensor probe for SARS-CoV-2 S protein. Si-doped ZnSeS quantum dots were synthesized and coated with carboxy SiO_2 and subsequently conjugated to an Apta-MB probe. Cationic AuNPs were bonded QDs-Apta-MB to form a QDs-Apta-MB-AuNP MEF biosensor probe that was used for enhanced detection of SARS-CoV-2 S protein. Electrochemical detection of SARS-CoV-2 S protein was carried out using the QDs-Apta-MB where DPV was used as the electrochemical detection technique. The electrode surface was characterized using CV, DPV and EIS whilst spectrophotometric, spectroscopic, fluorescence polarization and electron microscopy techniques were used to characterize the nanomaterials. We found $[Fe(CN)_6]/K^{3-}/^{4-}$ buffered with NaAc-KAc-TrizmaAc-KSCN-Borax as the appropriate electrolyte solution for SARS-CoV-2 S protein detection due to the unique projection of the QDs anodic peak. Ultralow concentration of SARS-CoV-2 S protein was selectively and quantitatively detected using the QDs-Apta-MB-AuNP MEF probe and the QDs-Apta-MB electrochemical probe. Detection of SARS-CoV-2 S protein in saliva was successfully accomplished using the QDs-Apta-MB-AuNP MEF probe.

CRediT authorship contribution statement

Oluwasesan Adegoke: Conceptualization, Investigation,

Methodology, Writing – original draft, Writing – review & editing, Funding acquisition. **Kayode Oyinlola:** Formal analysis, Writing – review & editing. **Ojodomo J. Achadu:** Formal analysis, Writing – review & editing. **Zhugen Yang:** Writing – review & editing.

Declaration of competing interest

The authors declare that they have no known competing financial interests or personal relationships that could have appeared to influence the work reported in this paper.

Data availability

Data will be made available on request.

Acknowledgements

OA acknowledge financial support from the Royal Society of Chemistry (RSC) through E22-7965264821 and the Engineering and Physical Sciences Research Council (EPSRC) through EP/X029956/1. OA is also grateful to the School of Science and Engineering, University of Dundee, for financial support and assistance with XRD and electron microscopy characterization of the nanomaterials. Financial support from the Leverhulme Trust through RC-2015-011 is acknowledged. OJA grateful acknowledges the funding received from the Seed Corn R&I Programme of the School of Health and Life Sciences, Teesside University.

Appendix A. Supplementary data

Supplementary data to this article can be found online at https://doi.org/10.1016/j.aca.2023.341926.

References

[1] S. Tajik, Z. Dourandish, K. Zhang, H. Beitollahi, Q.V. Le, H.W. Jang, M. Shokouhimehr, Carbon and graphene quantum dots: a review on syntheses, characterization, biological and sensing applications for neurotransmitter determination, RSC Adv. 10 (2020) 15406–15429.
[2] C.J. Barrelet, Y. Wu, D.C. Bell, C.M. Lieber, Synthesis of CdS and zns nanowires using single-source molecular precursors, J. Am. Chem. Soc. 125 (2003) 11498–11499.
[3] K.-T. Yong, W.-C. Law, I. Roy, Z. Jing, H. Huang, M.T. Swihart, P.N. Prasad, Aqueous phase synthesis of CdTe quantum dots for biophotonics, J. Biophot. 4 (2011) 9–20.
[4] M. Geszke-Moritz, M. Moritz, Quantum dots as versatile probes in medical sciences: synthesis, modification and properties, Mater. Sci. Eng. C 33 (2013) 1008–1021.
[5] G. Lu, Z. Yang, K. Zheng, S. Lin, J. Liu, B. Ye, J. Huang, Y. Zhang, Y. Ye, T. Guo, G. Chen, Metal-enhanced fluorescence of interlaminar composite film with self-assembled quantum Dots/Au@SiO_2 microarchitecture, Org. Electron. 77 (2020), 105540.
[6] J. Zhu, H. Chang, J.-J. Li, X. Li, J.-W. Zhao, Using silicon-coated gold nanoparticles to enhance the fluorescence of CdTe quantum dot and improve the sensing ability of mercury (II), Spectrochim. Acta Mol. Biomol. Spectrosc. 188 (2018) 170–178.
[7] K. Aslan, I. Gryczynski, J. Malicka, E. Matveeva, J.R. Lakowicz, C.D. Geddes, Metal-enhanced fluorescence: an emerging tool in biotechnology, Curr. Opin. Biotechnol. 16 (2005) 55–62.
[8] I. Gryczynski, J. Malicka, Y. Shen, Z. Gryczynski, J.R. Lakowicz, Multiphoton excitation of luorescence near metallic particles: enhanced and localized excitation, J. Phys. Chem. B 106 (2002) 2191–2195.
[9] O. Adegoke, M.-W. Seo, T. Kato, S. Kawahito, E.Y. Park, Gradient band gap engineered alloyed quaternary/ternary CdZnSeS/ZnSeS quantum dots: an ultrasensitive fluorescence reporter in a conjugated molecular beacon system for the biosensing of influenza virus RNA, J. Mater. Chem. B 4 (2016) 1489–1498.
[10] O. Adegoke, C. McKenzie, N. Nic Daeid, Multi-shaped cationic gold nanoparticle-L-cysteine-ZnSeS quantum dots hybrid nanozyme as an intrinsic peroxidase mimic for the rapid colorimetric detection of cocaine, Sensor. Actuator. B Chem. 287 (2019) 416–427.
[11] N. Liang, X. Hu, W. Li, A.W. Mwakosya, Z. Guo, Y. Xu, X. Huang, Z. Li, X. Zhang, X. Zou, J. Shi, Fluorescence and colorimetric dual-mode sensor for visual detection of malathion in cabbage based on carbon quantum dots and gold nanoparticles, Food Chem. 343 (2021), 128494.
[12] X. Tao, Z. Liao, Y. Zhang, F. Fua, M. Haoa, Y. Songa, E. Song, Aptamer-quantum dots and teicoplanin-gold nanoparticles constructed FRET sensor for sensitive detection of Staphylococcus aureus, Chin. Chem. Lett. 32 (2021) 791–795.
[13] Q. Liu, Y.-C. Yeh, S. Rana, Y. Jiang, L. Guo, V.M. Rotello, Differentiation of cancer cell type and phenotype using quantum dot-gold nanoparticle sensor arrays, Cancer Lett. 334 (2013) 196–201.
[14] T. Liu, N. Li, J.X. Dong, Y. Zhanga, Y.Z. Fan, S.M. Lin, H.Q. Luo, N.B. Li, A colorimetric and fluorometric dual-signal sensor for arginine detection by inhibiting the growth of gold nanoparticles/carbon quantum dots composite, Biosens. Bioelectron. 87 (2017) 772–778.
[15] P.M. Ndangili, A.M. Jijana, P.G.L. Baker, E.I. Iwuoha, 3-Mercaptopropionic acid capped ZnSe quantum dot-cytochrome P450 3A4 enzyme biotransducer for 17β-estradiol, J. Electroanal. Chem. 653 (2011) 67–74.
[16] N. Zhu, D. Zhang, W. Wang, X. Li, B. Yang, J. Song, X. Zhao, B. Huang, W. Shi, R. Lu, P. Niu, F. Zhan, X. Ma, D. Wang, W. Xu, G. Wu, G.F. Gao, W. Tan, A novel coronavirus from patients with pneumonia in China, N. Engl. J. Med. 382 (2019) 727–733.
[17] C. Wang, P.W. Horby, F.G. Hayden, G.F. Gao, A novel coronavirus outbreak of global health concern, Lancet 395 (2020) 470–473.
[18] J.F.W. Chan, S. Yuan, K.H. Kok, K.K.W. To, H. Chu, J. Yang, F. Xing, J. Liu, C.C.-Y. Yip, R.W.-S. Poon, H.-W. Tsoi, S.K.-F. Lo, K.-H. Chan, V.K.-M. Poon, W.-M. Chan, J.D. Ip, J.-P. Cai, V.C.-C. Cheng, H. Chen, C.K.-M. Hui, K.-Y. Yuen, A familial cluster of pneumonia associated with the 2019 novel coronavirus indicating persono-to-person transmission: a study of a family cluster, Lancet 395 (2020) 14–523.
[19] Weekly epidemiological update on COVID-19 - 3 August 2023. https://www.who.int/publications/m/item/weekly-epidemiological-update-on-covid-19—3-august-2023.
[20] L. Chen, W. Liu, Q. Zhang, K. Xu, G. Ye, W. Wu, Z. Sun, F. Liu, K. Wu, B. Zhong, Y. Mei, W. Zhang, Y. Chen, Y. Li, M. Shi, K. Lan, Y. Liu, RNA based mNGS approach identifies a novel human coronavirus from two individual pneumonia cases in 2019 Wuhan outbreak, Emerg. Microb. Infect. 9 (2020) 313–319.
[21] H. Yao, Y. Song, Y. Chen, N. Wu, J. Xu, C. Sun, J. Zhang, T. Weng, Z. Zhang, Z. Wu, L. Cheng, D. Shi, X. Lu, J. Lei, M. Crispin, Y. Shi, L. Li, S. Li, Molecular architecture of the SARSCoV-2 virus, Cell 183 (2020) 730–738, e13.
[22] N. Wang, J. Shang, S. Jiang, L. Du, Subunit vaccines against emerging pathogenic human coronaviruses, Front. Microbiol. 11 (2020) 298.
[23] M. Svobodova, V. Skouridou, M. Jauset-Rubio, I. Viéitez, A. Fernández-Villar, J.J. C. Alvargonzalez, E. Poveda, C.B. Bofill, T. Sans, A. Bashammakh, A.O. Alyoubi, C. K. O'Sullivan, Aptamer Sandwich assay for the detection of SARS-CoV-2 spike protein antigen, ACS Omega 6 (2021) 35657–35666.
[24] F. Li, W. Li, M. Farzan, S.C. Harrison, Structure of SARS coronavirus spike receptor-binding domain complexed with receptor, Science 309 (2005) 1864–1868.
[25] J. Lan, J. Ge, J. Yu, S. Shan, H. Zhou, S. Fan, Q. Zhang, X. Shi, Q. Wang, L. Zhang, X. Wang, Structure of the SARS-CoV-2 spike receptor-binding domain bound to the ACE2 receptor, Nature 581 (2020) 215–220.
[26] W. Tai, L. He, X. Zhang, J. Pu, D. Voronin, S. Jiang, Y. Zhou, L. Du, Characterization of the receptor-binding domain (RBD) of 2019 novel coronavirus: implication for development of RBD protein as a viral attachment inhibitor and vaccine, Cell. Mol. Immunol. 17 (2020) 613–620.
[27] L. Dai, G.F. Gao, Viral targets for vaccines against COVID-19, Nat. Rev. Immunol. 21 (2021) 3–82.
[28] H. Yan, L. Jiao, H. Wang, W. Xu, Y. Wu, W. Gu, D. Du, Y. Lin, C. Zhu, A "sense-and-treat" ELISA using zeolitic imidazolate framework-8 as carriers for dual-modal detection of carcinoembryonic antigen, Sensor. Actuator. B Chem. 297 (2019), 126760.
[29] B. Lorbetskie, T. White, M. Creskey, X. Zhang, M. Girard, R.Y. Tam, S. Sauve, H. Lu, Selective reversed-phase high-performance liquid chromatography method for the determination of intact SARS-CoV-2 spike protein, J. Chromatogr. A 1680 (2022), 463424.
[30] N. Bhalla, Y. Pan, Z. Yang, A.F. Payam, Opportunities and challenges for biosensors and nanoscale analytical tools for pandemics: COVID-19, ACS Nano 14 (2020) 7783–7807.
[31] H. Han, C. Wang, X. Yang, S. Zheng, X. Cheng, Z. Liu, B. Zhao, R. Xiao, Rapid field determination of SARS-CoV-2 by a colorimetric and fluorescent dual-functional lateral flow immunoassay biosensor, Sensor. Actuator. B Chem. 351 (2022), 130897.
[32] M. Barlev-Gross, S. Weiss, A. Ben-Shmuel, A. Sittner, K. Eden, N. Mazuz, I. Glinert, E. Bar-David, R. Puni, S. Amit, O. Kriger, O. Schuster, R. Alcalay, E. Makdasi, E. Epstein, T. Noy-Porat, R. Rosenfeld, H. Achdout, O. Mazor, T. Israely, H. Levy, A. Mechaly, Spike vs nucleocapsid SARS-CoV-2 antigen detection: application in nasopharyngeal swab specimens, Anal. Bioanal. Chem. 413 (2021) 3501–3510.
[33] I.C. Samper, C.J. McMahon, M.S. Schenkel, K.M. Clark, W. Khamcharoen, L.B. R. Anderson, J.S. Terry, E.N. Gallichotte, G.D. Ebel, B.J. Geiss, D.S. Dandy, C. S. Henry, Electrochemical immunoassay for the detection of SARS-CoV-2 nucleocapsid protein in nasopharyngeal samples, Anal. Chem. 94 (2022) 4712–4719.
[34] C. Dai, M. Guo, Y. Wu, B.-P. Cao, X. Wang, Y. Wu, H. Kang, D. Kong, Z. Zhu, T. Ying, y. Liu, D. Wei, Ultraprecise antigen 10-in-1 pool testing by multiantibodies transistor assay, J. Am. Chem. Soc. 143 (2021), 19794−19801.
[35] A. Scohy, A. Anantharajah, M. Bodéus, B. Kabamba-Mukadi, A. Verroken, H. Rodriguez-Villalobos, Low performance of rapid antigen detection test as frontline testing for COVID-19 diagnosis, J. Clin. Virol. 129 (2020), 104455.
[36] Y.W. Tang, J.E. Schmitz, D.H. Persing, C.W. Stratton, Laboratory diagnosis of COVID-19: current issues and challenges, J. Clin. Microbiol. 58 (2020) 10–1128.
[37] S.J. Zhen, L.Q. Chen, S.J. Xiao, Y.F. Li, P.P. Hu, L. Zhan, L. Peng, E.Q. Song, C. Z. Huang, Carbon nanotubes as a low background signal platform for a molecular aptamer beacon on the basis of long-range resonance energy transfer, Anal. Chem. 82 (2010) 8432–8437.

[38] G. Yang, Z. Li, I. Mohammed, L. Zhao, W. Wei, H. Xiao, W. Guo, Y. Zhao, F. Qu, Y. Huang, Identification of SARS-CoV-2-against aptamer with high neutralization activity by blocking the RBD domain of spike protein 1, Signal Transduct. Target Ther. 6 (2021) 227.
[39] S.J. Lim, M.U. Zahid, P. Le, L. Ma, D. Entenberg, A.S. Harney, J. Condeelis, A. M. Smith, Brightness-equalized quantum dots, Nat. Commun. 6 (2015) 8210.
[40] L. Qu, X.G. Peng, Control of photoluminescence properties of CdSe nanocrystals in growth, J. Am. Chem. Soc. 124 (2002) 2049–2055.
[41] K. Park, M.-s. Hsiao, Y.-J. Yi, S. Izor, H. Koerner, A. Jawaid, R.A. Vaia, Highly concentrated seed-mediated synthesis of monodispersed gold nanorods, ACS Appl. Mater. Interfaces 9 (2017) 26363–26371.
[42] D.V. Talapin, I. Mekis, S. Go1tzinger, A. Kornowski, O. Benson, H. Weller, CdSe/CdS/ZnS and CdSe/ZnSe/ZnS core-shell-shell nanocrystals, J. Phys. Chem. B 108 (2004) 18826–18831.
[43] E. Rafiee, S. Shahebrahimi, M. Feyzi, M. Shaterzadeh, Optimization of synthesis and characterization of nanosilica produced from rice husk (a common waste material), Int. Nano Lett. 2 (2012) 29.
[44] I.S. Elashmawi, N.A. Hakeem, M.S. Selim, Optimization and spectroscopic studies of CdS/poly(vinyl alcohol) nanocomposites, Mater. Chem. Phys. 115 (2009) 132–135.
[45] O. Adegoke, H. Montaseri, S.A. Nsibande, P.B.C. Forbes, Passivating effect of ternary alloyed AgZnSe shell layer on the structural and luminescent properties of CdS quantum dots, Mater. Sci. Semicond. Process. 90 (2019) 162–170.
[46] N.J. Moerke, Fluorescence polarization (FP) assays for monitoring peptide-protein or nucleic acid–protein binding, Curr. Protoc. Mol. Biol. 1 (2009) 1–15.
[47] J. Lipfert, S. Doniach, R. Das, D. Herschlag, Understanding nucleic acid–ion interactions, Annu. Rev. Biochem. 83 (2014) 813–841.
[48] R.W. Murray, Nanoelectrochemistry: metal nanoparticles, nanoelectrodes, and nanopores, Chem. Rev. 108 (2008) 2688–2720.